Design and Construction of a High Vacuum Surface Analysis Instrument to Study Chemistry at Nanoparticulate Surfaces

Brandon Reed Jeffery

Thesis submitted to the faculty of the Virginia Polytechnic Institute and State University
in partial fulfillment of the requirements for the degree of

Master of Science
In
Chemistry

John R. Morris, Chair
Gary L. Long
Brian M. Tissue

April 21, 2011
Blacksburg, VA

Keywords: nanoparticles, high vacuum, infrared spectroscopy, temperature programmed desorption, silicon dioxide, chemical warfare agent

Design and Construction of a High Vacuum Surface Analysis Instrument to Study Chemistry at Nanoparticulate Surfaces

Brandon Reed Jeffery

ABSTRACT

Metal oxide and metal oxide-supported metal nanoparticles can adsorb and decompose chemical warfare agents (CWAs) and their simulants. Nanoparticle activity depends on several factors including chemical composition, particle size, and support, resulting in a vast number of materials with potential applications in CWA decontamination. Current instrumentation in our laboratory used to investigate fundamental gas-surface interactions require extensive time and effort to achieve operating conditions.

This thesis describes the design and construction of a high-throughput, high vacuum surface analysis instrument capable of studying interactions between CWA simulants and nanoparticulate surfaces. The new instrument is small, relatively inexpensive, and easy to use, allowing for expeditious investigations of fundamental interactions between gasses and nanoparticulate samples. The instrument maintains the sample under high vacuum (10^{-7}-10^{-9} torr) and can reach operating pressures in less than one hour. Thermal control of the sample from 150-800 K enables sample cleaning and thermal desorption experiments. Infrared spectroscopic and mass spectrometric methods are used concurrently to study gas-surface interactions. Temperature programmed desorption is used to estimate binding strength of adsorbed species. Initial studies were conducted to assess the performance of the instrument and to investigate interactions between the CWA simulant dimethyl methylphosphonate (DMMP) and nanoparticulate silicon dioxide.

ACKNOWLEDGEMENTS

I would like to thank my advisor, Professor John Morris, for his assistance and encouragement throughout my career as a graduate student, as well as the opportunity to be part of the Morris Research Group. I would also like to acknowledge Professor Gary Long and Professor Brian Tissue for their help with my research and the writing of this thesis. Special thanks are due to Dimitar Panayotov for his invaluable assistance in the completion of my work and many helpful discussions, as well as Wes Gordon for teaching me about building vacuum instruments. Past and present members of the Morris group also deserve thanks for their help and for providing an enjoyable place to work.

I am extremely fortunate to have a great network of friends who have provided encouragement and support, including: Alec Wagner, Travis White, Amy Weber, Simon Taxel, Hikmat Daghestani, Chris Stetson, Michael Mobilia, and the Blacksburg Rugby Football Club. Finally, I would especially like to thank my family, Jay, Kathy, Drew, and Laura.

Table of Contents

LIST OF FIGURES

LIST OF TABLES

LIST OF ACRONYMS

AP-	Aerogel Prepared
CP-	Conventionally Prepared
CW	Chemical Weapon
CWA	Chemical Warfare Agent
DFP	Diisopropyl Fluorophosphate
DIMP	Diisopropyl Methylphosphonate
DMMP	Dimethyl Methylphosphonate
DPMP	Diphenyl Methylphosphonate
ECBC	Edgewood Chemical Biological Center
FT-IR	Fourier Transform Infrared
IR	Infrared
MAS	Magic Angle Spinning
MCT	Mercury-Cadmium-Telluride
MDCP	Methyl Dichlorophosphate
MMP	Methyl Methylphosphonate
MP	Methyl Phosphonate
MS	Mass Spectrometry
NMR	Nuclear Magnetic Resonance
OFHC	Oxygen Free High Conductivity
PID	Proportional-Integral-Derivative
QCM	Quartz Crystal Microbalance
RGA	Residual Gas Analyzer
TCP	Trichlorophosphate
TMP	Trimethylphosphate
TPD	Temperature Programmed Desorption
UHV	Ultrahigh Vacuum
UV	Ultraviolet
VCR	Vacuum Coupling Radiation
XPS	X-ray Photoelectron Spectroscopy

Chapter 1: Background and Motivation

1.1 Introduction

The decontamination of chemical warfare agents is of great importance to both the military and civilian first responders. Conventional, solution-phase decontamination methods can be inefficient or ineffective. Metal oxides and metal oxide nanoparticles have shown promise as effective decontamination reactants that do not possess the shortcomings of solution-based strategies. In particular, gold nanoparticles supported on titania show high activity for the adsorption and decomposition of the chemical warfare agent simulant dimethyl methylphosphonate (DMMP). However, transition metal nanoparticles supported on metal oxides have not been investigated extensively. In addition to the elements used for the metal and metal oxide support, nanoparticle size affects the activity of the system. The permutations of metal, metal oxide support, and particle size comprise a vast number of combinations of materials that could decompose chemical warfare agents. **To investigate the ability of nanoparticulate transition metal-metal oxide surfaces to decompose chemical warfare agent simulants, I designed and constructed a high-throughput high vacuum instrument capable of studying gas-surface interactions.**

Current methods to study the activity of metal nanoparticle/metal oxide surfaces require extensive time and effort to achieve ideal operating conditions after introducing the sample to the instrument. I developed a high-throughput instrument that minimizes sample loading time and surface preparation while maintaining the ability to utilize an array of surface instrumentation including temperature programmed desorption, mass spectrometry, and infrared spectroscopy. This instrument was designed to minimize cost and laboratory footprint while maintaining functionality and the potential to be used for other applications.

Using the ability of the new instrument to gather information on DMMP adsorption and decomposition on many different surfaces, we will identify metal oxide-supported transition metal nanoparticle combinations that possess superior uptake and decomposition activity towards DMMP and other chemical warfare agent simulants. In addition, we will elucidate the mechanism of adsorption and decomposition of chemical warfare agent simulants on various surfaces and factors that affect the efficacy of the material as a destructive sorbent. By understanding the fundamental aspects of the reaction, it will be possible to identify materials that would function most effectively as chemical warfare agent decontamination methods.

1.2 Background

1.2.1 Chemical Warfare Agents

While many weapons in the world today derive their destructive power from some sort of chemical reaction, the term "chemical warfare agent" has a much more confined definition. Conventional explosives employ combustion reactions and even nuclear bombs exploit the physical properties of certain chemicals. However, the term "chemical weapon" (CW) or "chemical warfare agent" (CWA) generally refers to a substance or precursor whose toxic properties are used to cause harm or death to an enemy.[1] Although the use of chemical weapons dates back to 2000 BC, the history of modern CWAs begins with World War I when Germany and Britain weaponized and deployed chlorine, mustard, Lewisite, and several other chemicals. Most of these gasses were vesicants (blister agents) or asphyxiants (choking agents).
The development of such chemicals continued and, while researching insecticides in 1936, German scientist Gerhardt Schräder discovered a particularly toxic compound that he called Tabun, also known as "GA". The discovery of similar organophosphorus compounds Sarin

(GB) and Soman (GD) soon followed. Generally referred to as nerve agents, the increased lethality of these organophosphorus compounds is due to their toxic pathway.[2] This exceptionally lethal class of chemical weapons was augmented by the discovery of the V-series agents, which were significantly more toxic and persistent than Sarin. The "V" designation comes from "venomous" due to the agents' similarities to snake venom. In 1957, after synthesizing and testing roughly fifty V-series agents, the United States Army Research and Development Command decided VX afforded the most military advantages and chose to focus research towards the development of this compound.[3]

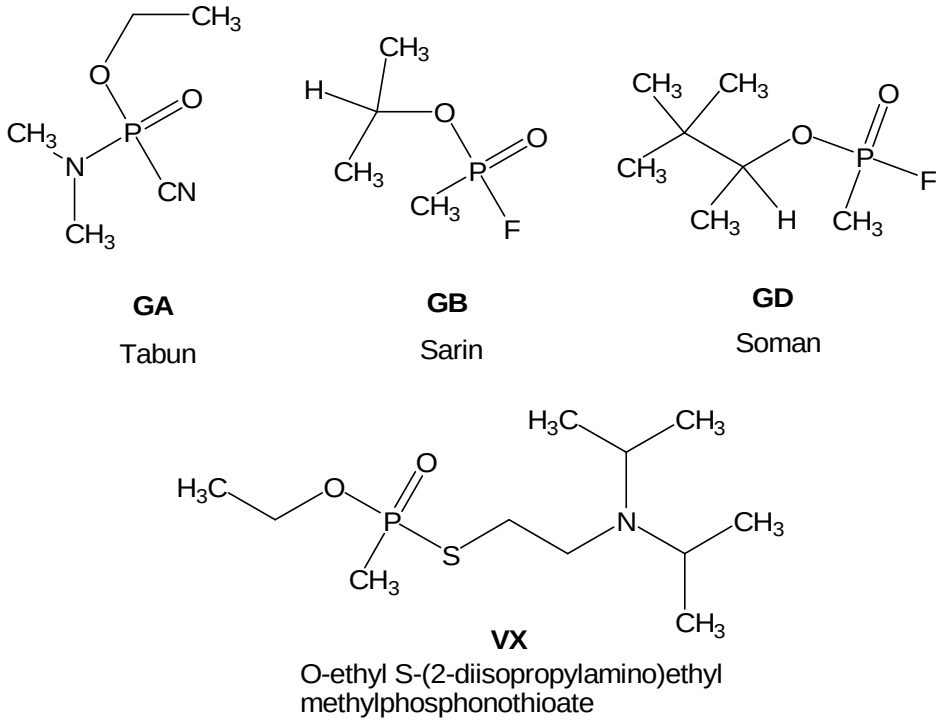

Figure 1.1: Structures of four common nerve agents.

Both G and V agents are classified as nerve agents and have a similar mechanism of toxicity as other organophosphorus pesticides. Nerve agents are considered to be the most toxic

CWAs and work as acetylcholinesterase inhibitors. The nerve agent phosphorylates the active center of acetylcholinesterase, which causes the enzyme to undergo irreversible dealkylation. This inhibition of the enzyme results in increased levels of acetylcholine causing loss of control of central nervous system and musculoskeletal functions, the symptoms of which can range from rhinorrhea to death.[4] Other symptoms include miosis, headache, dyspnea, convulsions, syncope, loss of bladder and bowel control, respiratory arrest, and paralysis, among others.[2]

Table 1.1: Toxicity of Nerve Agents. [a]Lethal concentration, [b]incapacitating concentration, [c]concentration to trigger first noticeable symptoms, and [d]lethal dose for percutaneous exposure for the median population.

Agent	LCt_{50} (mg·min/m^3) [a]	ICt_{50}(mg·min/m^3) [b]	MCt_{50}(mg·min/m^3) [c]	LD_{50}(mg) [d]
GA	400	n/a	-	1700
GB	100	75	<1	1700
GD	70	n/a	<1	50
VX	50	35	0.04	10

With the increase of international terrorism, the threat of CWA attacks must be taken seriously. Political instability has led to both the emergence of terrorist groups and availability of CWAs or their precursors. Unlike nuclear devices, specialized equipment and rare materials are not necessary to produce CWAs. The Sarin attacks in Japan in 1994 and 1995 and the use of nerve agents by Iraq in the Iran-Iraq war are clear evidence that CWA attacks are a pertinent threat in both domestic and military situations.[3, 5] While the threat of a chemical attack on military forces is of great concern, the potential for terrorist attacks on civilian populations further underscores the need for decontamination and detection procedures for first responders. In addition to decontamination in response to a CWA attack, the demilitarization of stockpiles is

also of concern.[6-8] The current methods of stockpile destruction are incineration and neutralization, which can be expensive, problematic, and inefficient.[9-11]

1.2.2 Decontamination of CWAs

Presently, basic chlorine and peroxide solutions are the conventional method of CWA decontamination. In addition to being heavy and not easily transportable, many decontamination solutions are corrosive and are not compatible with electrical equipment, skin, clothing, and various paints, metals, and polymers.[2, 11] Furthermore, some CWAs are resistant to a certain decontamination formula or react with the decontamination solution to form toxic byproducts. Solution-phase decontamination procedures are not preventative and are only effective when applied after exposure to a CWA.

Decontamination methods that involve solid materials are being investigated to circumvent the shortcomings of solution-phase procedures. The use of solid-state decontaminants increases portability, decreases weight, and could potentially be incorporated into coatings or paints and applied to equipment, thereby making the equipment itself resistant to contamination by CWAs. In particular, metal oxides and metal oxide nanoparticles have been shown to be effective CWA sorbents and to catalytically and non-catalytically decompose the CWA simulants.

1.2.3 CWA Simulants

An obvious hindrance to studying CWAs is their high level of toxicity. To overcome this problem, molecules that possess similar physical and chemical properties, but are significantly less toxic, are used to mimic certain properties of CWAs. By maintaining some of the same key functional groups, the simulants can be used to study the interactions between CWAs and prospective decontaminants without the inherent danger associated with the real agent. Due to

its low toxicity, similar vapor pressure, and important P=O, P-O-C, and P-C bonds, the simulant dimethyl methylphosphonate (DMMP) is a common mimic for Sarin.[9] Although its structural and physical properties are less similar, DMMP is also used to mimic other nerve agents such as Tabun, Soman, and VX. Figure 1.2 shows the structure of DMMP and other common CWA simulants. Table 2.2 shows the physical properties of Sarin and CWA simulants.

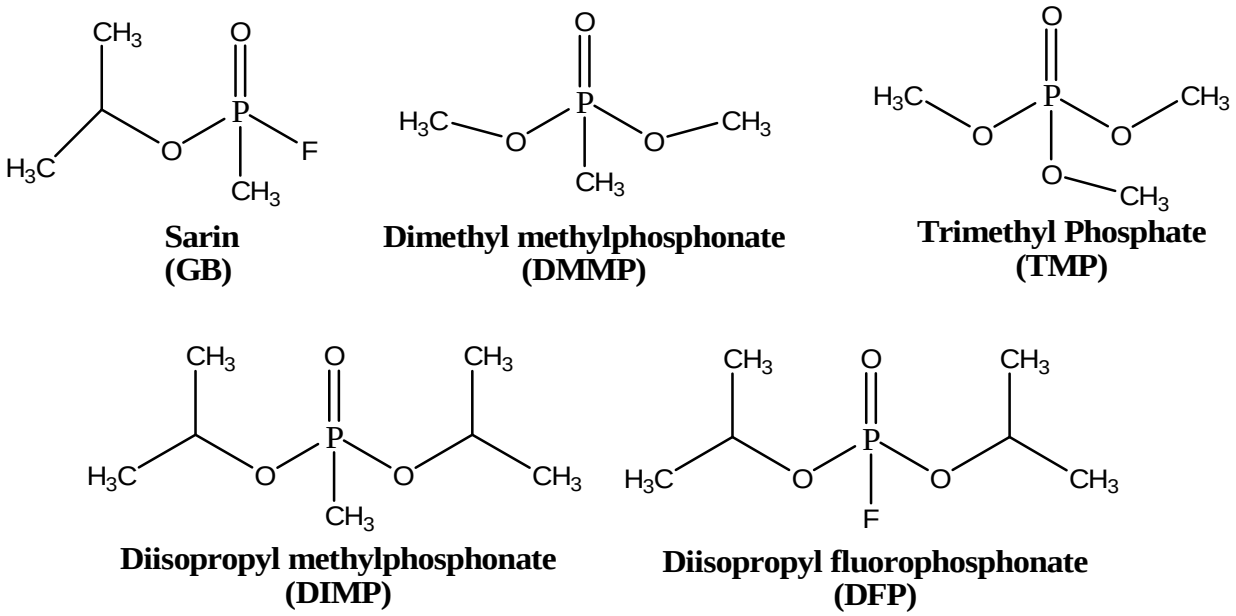

Figure 1.2: Structure of Sarin and CWA simulants.

Table 1.2: Physical properties of Sarin (GB) and CWA simulants.[12]

Compound	Molecular Weight (g/mol)	Melting Point (K)	Boiling Point (K)	Vapor Pressure (mm Hg)	LD_{50}, Rat oral (mg/kg)
GB	***140.1***	***219***	***433***	***2.1***	***0.55***
DMMP	124.08	---	454	0.96	8,210
DIMP	180.18	298	---	0.277	826
TMP	140.08	227	470	0.85	840
DFP	184.15	213	458	0.58	5

1.2.4 Nanoparticles

Nanoparticles possess different properties than their corresponding bulk material for a variety of reasons.[13] Nanomaterials exhibit a high surface area to bulk ratio and possess high concentrations of defect sites, corners, and edges that can increase reactivity. Such materials also display acid-base character different from that of the bulk material. Nanoparticles exhibit properties divergent from surfaces comprised of the correlating bulk material. Since the reactive sites and edges of nanomaterials are defined by three dimensions, the size and shape of the nanomaterial become very important to their properties and reactivity.[14] The dramatic increase in surface atoms as particle size decreases is shown by Figure 1.3.[15] Due to the increased surface area and number of active sites, nanoparticles are of significant interest as potential sorbents for CWAs.

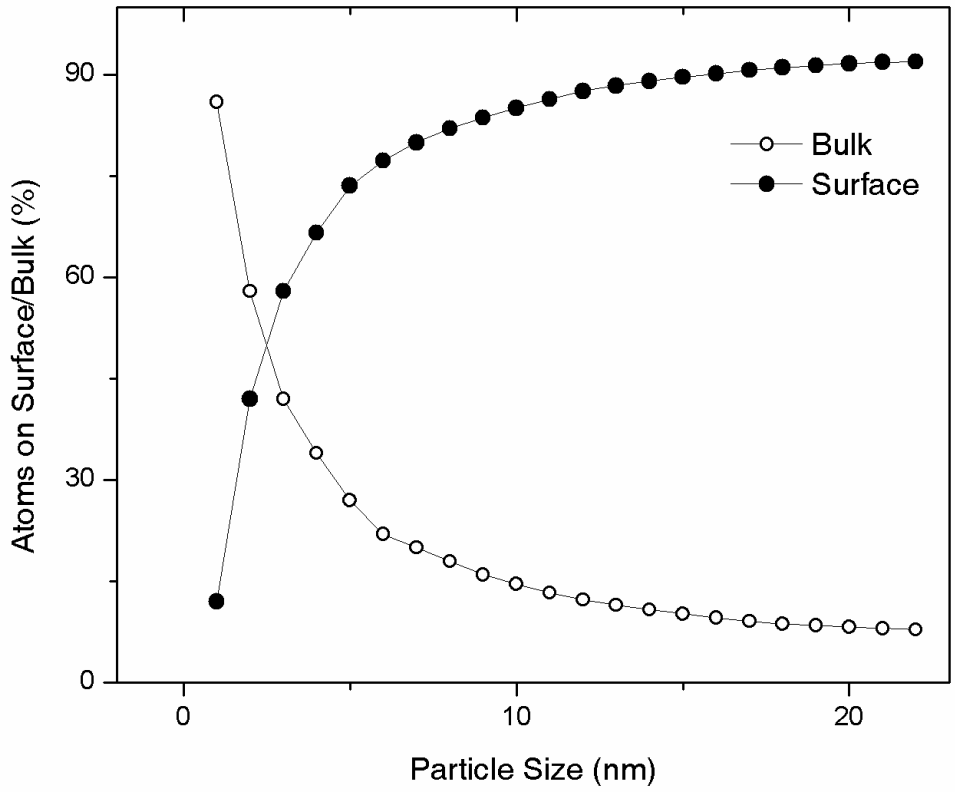

Figure 1.3: Particle size versus atom distribution.[15]

1.3 Metal Oxides as Solid Sorbents for Chemical Warfare Agents (and Simulants)

Given the deficiencies of solution based decontamination methods, there is much interest in metal oxides, which have shown promise in adsorbing and decomposing CWAs. Nanoparticulate metal oxides have been shown to be more active than bulk materials in decomposing organophosphorus compounds.[15] Metal oxide nanoparticles supported on other metal oxides have also been investigated.[16] Recent studies have demonstrated catalytic degradation of DMMP by titania-supported gold nanoparticles.[17]

1.3.1 Metal Oxides

In 1985, Templeton and Weinberg investigated the adsorption and decomposition of DMMP on alumina. They discovered that alumina would decompose DMMP at temperatures above 295 K. Diisopropyl methylphosphonate (DIMP) and diphenyl methylphosphonate (DPMP) were also found to adsorb dissociatively at or above 295 K. Templeton and Weinberg proposed that phosphonate esters could react with the surface hydroxyls (Bronsted acid site) or coordinatively unsaturated aluminum (Lewis acid site) as seen in Figure 1.4. They concluded at 200 K, a weakly chemisorbed state exists between DMMP and the surface hydroxyl (Figure 1.4(A)). Above 295 K, DMMP adsorbs dissociatively via the coordinatively unsaturated site to form the adspecies methyl methylphosphonate (MMP) as shown in Figure 1.5, with the methoxy species either remaining bound to the surface as methoxide or leaving as methanol.[18, 19] Kuiper et al. discovered that Sarin also adsorbed to γ-alumina Lewis acid sites through the oxygen on the P=O bond.[20, 21]

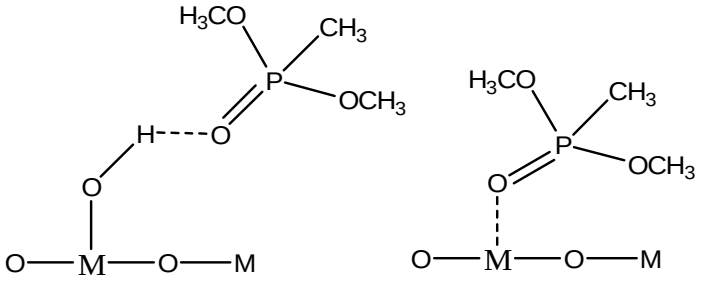

Figure 1.4: DMMP adsorption sites on Al_2O_3 showing (a) Hydrogen bonding of DMMP to surface hydroxyl and (b) bonding of DMMP to a Lewis acid site. [18, 19]

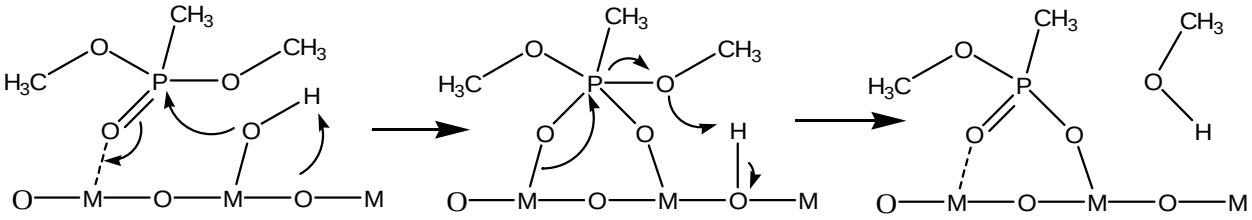

Figure 1.5: Proposed mechanism for the decomposition of DMMP on a metal oxide surface.[18, 19]

Henderson et al.[22] determined that while Fe_2O_3 would decompose DMMP at temperatures as low as 250 K, dehydrated silicon dioxide would not decompose DMMP before the DMMP desorbed. On hydrated silica, DMMP decomposition of only 10% of a monolayer was detected.[22] Mitchell et al. used infrared (IR) spectroscopy to study the adsorption and decomposition of DMMP on alumina.[23] Their study confirms the initial binding of the P=O species to the surface, as well as the loss of one methoxy group by 473 K, resulting in MMP adsorbed to the surface. At temperatures exceeding 573 K, the loss of a second methoxy group is observed resulting in methylphosphonate (MP), which remains adsorbed and intact after exposure to 70 torr of oxygen at 673 K. The study also examines DMMP adsorption on MgO and La_2O_3 which supports similar reactions resulting in the loss of the methoxy groups while the MP species remains bound to the surface. Investigations by Lin and Klabunde[24] support the mechanism proposed by Mitchell for the adsorption and decomposition of DMMP on magnesia. The study also confirms that the reaction is stoichiometric and not catalytic with no detectable desorption of methylphosphonate, even at high temperatures.

When Mitchell et al. looked at iron oxide,[23] significant differences in the mechanism of adsorption and decomposition were observed. Instead of seeing the loss of one methoxy at a

time, no methyl stretches were apparent above 573 K indicating no selectivity towards a certain methoxy group. Furthermore, the elimination of the phosphorus bound methyl was observed on Fe_2O_3,[23] a bond that remained intact when DMMP was adsorbed on the other metal oxide surfaces. The absence of any adsorbed carbon-containing species is in concordance with a study by Henderson[22] which used temperature programmed desorption (TPD) and Auger electron spectroscopy (AES) to study interactions of DMMP with Fe_2O_3. Mitchell also did not detect any phosphorus species desorbing from the Fe_2O_3 surface.[23] The decomposition mechanism for iron oxide (Figure 1.6) is different than other metal oxides and is of interest due to the lower temperature needed for decomposition and because no oxygen is needed to break the P-CH_3 bond.

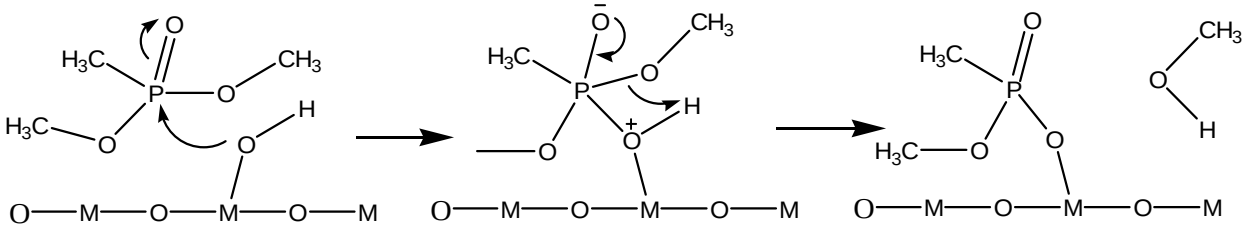

Figure 1.6: Nucleophilic attack of Iron Oxide on DMMP[23]

By comparing the reduction potentials for the metals in this study, it becomes apparent why iron oxide reacts via a different mechanism (Table 1.3). The higher reduction potential for iron oxide results in multiple available oxidation states, Fe(II) and Fe(III), and enables iron oxide to act as an oxidation catalyst as shown in Equations 1.1-1.3.[23]

Table 1.3: Reduction potentials.[23] [a]Compared to standard hydrogen electrode

Reaction	Reduction Potential[a] (V)
$Fe^{3+} + e^- \rightarrow Fe^{2+}$	0.77
$Al^{3+} + 3e^- \rightarrow Al$	−1.66
$Mg^{2+} + 2e^- \rightarrow Mg$	−2.36
$La^{3+} + 3e^- \rightarrow La$	−2.52

$$Fe_2O_3 + 2e^- \rightarrow 2\ FeO + O^{2-} \quad (1.1)$$

$$(H_3CO)_2P(O)CH_3 + O^{2-} \rightarrow (H_3CO)_2P(O)^-_{ads} + H_3CO^-_{ads} \quad (1.2)$$

$$2\ FeO + ½\ O_2 \rightarrow Fe_2O_3 \quad (1.3)$$

Titania is another metal oxide that has garnered much attention in the decomposition of DMMP. Rusu and Yates used IR spectroscopy to study the adsorption and decomposition of DMMP on TiO_2 and proposed three possible adsorption mechanisms (Figure 1.7).[25] When DMMP was exposed to titania, a frequency shift in the P=O IR absorption band was observed. Notably, this was not accompanied by a shift in the $\nu_{c\text{-}o}$ absorption indicating that structures (A) or (B) are more likely than structure (C).

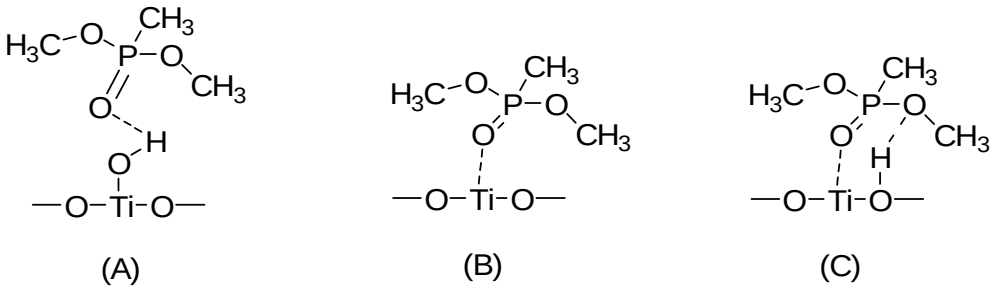

Figure 1.7: Possible adsorption schemes for DMMP on TiO_2 showing DMMP (A) hydrogen bonded to a surface hydroxyl, (B) bonded to a Lewis acid site, and (C) bonded through the phosphoryl oxygen and hydrogen bonded through the methoxy oxygen.[25]

This adsorption scheme agrees with Templeton and Weinberg's findings for DMMP on Al_2O_3, La_2O_3, and MgO and supports their proposed decomposition mechanism for temperatures greater than 214 K.[18, 19]

Obee and Satyapal[26] reported photocatalytic decomposition of DMMP on TiO_2. It is generally reported that irradiation of TiO_2 with ultraviolet light promotes a valence electron to the conduction band (e_c^-). The conduction band electron is capable of reducing an adsorbed species, concurrently forming a valence band hole (h_v^+) (Equation 1.4) which can oxidize an adsorbed species.[27, 28] The conduction band electron can react with adsorbed O_2 to produce a superoxide (Equation 1.5)[28] and the valence band hole can react with water to produce hydroxyl radicals (Equation 1.6).[28] The conduction band electron, valence hole, superoxide or hydroxyl radicals could potentially react with an adsorbed organic species such as DMMP.

$$TiO_2 + h\nu \rightarrow e_c^- + h_v^+ \quad (1.4)$$

$$e_c^- + O_2 \rightarrow O_2^- \quad (1.5)$$

$$h_v^+ + H_2O \rightarrow H^+ + {}^{\bullet}OH \quad (1.6)$$

DMMP was decomposed on titania in the presence of UV at room temperature but the surface was deactivated by phosphates and methyl phosphonic acid, products of DMMP decomposition. However, Obee and Satyapal reported complete regeneration of the catalyst only after washing the surface with water.[26]

Table 1.4: Summary of DMMP on Metal Oxides

Surface	Products/Observations	Conclusions
MgO	Adsorbed O-P-O species @ high T, little O-P-O at RT	adsorbs through P=O[24]
MgO	Little difference in IR between 773 and 973	P=O adsorbs to Lewis acid site (metal)[29]
MgO	Adsorbed MP @ high T	Stoichiometric decomposition[24]
Al_2O_3	$-OCH_3$, adsorbed MMP	Adsorbs to surface via P=O
Al_2O_3	Adsorbed MP @ T > 573 K in 70 torr O_2	MP species poisons surface
Fe_2O_3	Loss of methoxy @ 170 K, no observed intact P-CH_3 bond @ 250 K	DMMP decomposes at lower temperatures, different mechanism possible[18, 19]
Fe_2O_3	No desorbed P observed	P poisons surface[23]
SiO_2 (dehydroxylated)	No decomposition products	DMMP desorbs molecularly before decomposition[22, 23]
SiO_2 (hydrated)	DMMP adsorbs molecularly	Minimal decomposition[22]
TiO_2	No shift in ν_{c-o} upon adsorption	Hydrogen bonding to surface through P-O-CH_3 not likely[25]
TiO_2	Methanol, adsorbed O-P-O bridging species	Similar mechanism to other metal oxides, faster decomposition, photoactive[25, 26, 30]

1.3.2 Metal Oxide Supports

The decomposition of DMMP has also been studied on various metal oxides and metals supported on other metal oxides. Graven et al. reported the oxidation of DMMP on an alumina-supported platinum surface.[31] Segal et al. observed high DMMP decomposition activity of Mn/Al_2O_3 and amorphous manganese oxide ($K_{0.6}Mn_{0.93}O_2$, Mn oxidation state 3.5-3.6)[32] on Al_2O_3 at temperatures from 473 to 673 K.[33] Cao et al. examined the ability of nickel, iron, copper, and vanadium-supported on Al_2O_3, SiO_2, and TiO_2 to thermocatalytically decompose

DMMP.[34] They determined vanadium outperformed Graven's Pt/Al_2O_3 catalyst and all other catalysts examined in their study. Due to its high surface area and inactivity towards DMMP oxidation, silica was determined to be the optimal support. Because DMMP desorbs from SiO_2 before decomposition occurs,[22] the silica was not occluded by phosphorus containing DMMP decomposition products. Although very effective at degrading DMMP, the vanadium/silica catalyst requires temperatures of 723 K to maintain this efficiency.

Mitchell and Sheinker continued investigations of metal oxide-supported materials by comparing reactivity of γ-Al_2O_3, FeO_x/Al_2O_3, and sol-gel prepared Al_2O_3.[35] All materials studied decomposed DMMP at room temperature and the rate of decomposition increased with temperature. The alumina-supported iron oxide displayed a decomposition rate of almost twice that of the alumina and showed greater activity than other surfaces at higher temperatures.[35] The alumina-supported iron oxide also exhibited greater reaction sustainability, possibly due to the formation of an iron-aluminum phosphate with strong acid-base character.[36] The sol-gel prepared alumina exhibited an even higher initial activity, with decomposition rates of approximately twice that of the other surfaces. However, the activity of sol-gel alumina was reduced more rapidly and at an earlier point than alumina and alumina-supported iron oxide, presumably due to increased surface area.[35]

Mitchell et al.[8] further investigated the activity of metal oxide-supported particles. Iron oxide on alumina and cerium oxide on alumina both show increased reactivity compared to pure alumina. At room temperature, cerium oxide and iron oxide co-impregnated alumina (iron and cerium at 5 and 7.5% by weight, respectively) demonstrated an activity 2.5 times greater than any previously investigated surface.[8]

1.3.3 Metal Oxide Nanoparticles

Li and Klabunde investigated the potential of nanoscale MgO as a destructive sorbent for DMMP and found that one molecule of DMMP was adsorbed for every two available surface sites, demonstrating the reaction was stoichiometric.[29] Klabunde et al. discovered that MgO and CaO nanoparticles exhibited a higher activity than the corresponding bulk materials towards the destructive adsorption of DMMP and other small molecules.[15] In addition to comparing nanoparticles to bulk metal oxides, two methods of nanoparticle preparation were used: autoclave or aerogel prepared (AP-) and conventionally prepared (CP-). The smaller sized AP-metal oxides exhibited higher adsorption activity than the larger CP-metal oxides. The activity of these materials was also shown to be enhanced by various transition metal oxides adsorbed to the MgO and CaO nanoparticles.[15] The Klabunde group continued their investigations with MgO and CaO nanoparticles coated with first-row transition metal oxides. The study of these so-called "core-shell" nanoparticles supported earlier data demonstrating enhanced activity of MgO and CaO when impregnated with transition metal oxides.[16] The study also underscored the importance of small particle size in increasing sorbent activity. Although not observed for DMMP, the group claims to have discovered catalytic activity of supported Fe_2O_3 in the decomposition of CCl_4. While the adsorption is not stoichiometric, the surface appears to be regenerated by an ion-ion exchange between the Fe_2O_3 shell and the metal oxide core.[16] Further research in the Klabunde group by Decker et al. accented the importance of CaO particle size in the activity of destructive adsorption of DMMP.[37] The aforementioned studies, however, only investigated DMMP decomposition at 473 K and up. Nanoscale titania, as well as other nanocrystalline metal oxides, has also been shown to be an effective destructive sorbent of halocarbons.[13]

George Wagner et al. at the U.S. Army Edgewood Chemical Biological Center used solid-state magic angle spinning (MAS) NMR to investigate reactions of actual CWAs VX, GD, and HD with AP-CaO and AP- MgO. The nanoparticles were found to be an active sorbent at room-temperature, hydrolyzing VX and GD to form methylphosphonic acid, and HD to form divinyl sulfide or thiodiglycol.[38, 39] Wagner also demonstrated that VX, GB, and GD undergo hydrolysis on AP-Al_2O_3 at room temperature to form bulk aluminophosphonate complexes.[6] In addition to providing insight into the behavior of organophosphonates on nanoparticles, Wagner's studies affirm DMMP possesses enough similarities to actual CWAs to be a reasonable mimic to further investigate certain aspects of the destructive adsorption capabilities of nanoscale metal oxides.

Although many materials are effective in adsorbing and decomposing organophosphates, certain conditions are necessary which make the material impractical for many applications, most notably including decontamination. Decomposition of DMMP on various metal oxides, supported metal oxides, and nanoparticles typically requires elevated temperatures, well above ambient conditions. Titania is a promising material for a variety of CWA neutralization applications. However, as discussed previously, UV irradiation is necessary at room temperature to promote valence electrons to the conduction band in order to form the highly reactive superoxide and valence hole that participate in the decomposition of adsorbed organophosphates. Decomposition of DMMP and other organophosphates has also been shown to poison the catalyst via accumulation of adsorbed phosphorus species that do not undergo further oxidation or desorb, even at very high temperatures in the presence of oxygen.

1.3.4 Transition Metal Nanoparticles

Despite bulk gold's highly inert chemical properties, gold nanoparticles exhibit high catalytic activity when deposited on metal oxides.[40] Metal oxide-supported gold nanoparticles can actively decompose a variety of small molecules catalytically at room temperature or below.[41, 42] It has been proposed that the catalytic oxidation of such molecules is driven by superoxo (O_2^-) or peroxo (O_2^{-2}) species and that this occurs on the boundary of Au nanoparticles and the TiO_2 surface.[43] The mechanism of CO oxidation on Au/TiO_2 surfaces is contested and while CO is clearly different than DMMP, it can provide some insight as to the oxidative properties of titania-supported gold nanoparticles. While it is believed that atomic oxygen adsorbed on gold reacts with adsorbed CO, the nature of the reactive oxygen intermediate is not established.[44] Boccuzzi et al.[45] suggest two possible pathways: a slower one, induced by gas-phase oxygen and involving lattice oxygen, and a more rapid one where CO oxidation involves only oxygen from the gas-phase and occurs on the gold particles. Given the high activity observed for the Au/TiO_2 surface, they propose that the slower, lattice oxygen pathway plays a less significant role. Min and Friend claim that while the dissociation of molecular oxygen is the rate-limiting step, the oxidation of CO occurs most rapidly by atomic oxygen. The formation of atomic oxygen could be assisted by coordinatively unsaturated gold atoms, or a direct reaction of CO with molecular oxygen could form both CO_2 and an adsorbed oxygen species.[44] The role of lattice oxygen has also been disputed, but Chiorino et al. claim their experimental results are clear evidence that the lattice oxygen does not play a role in CO oxidation.[46] When CO adsorbed on Au/TiO_2 was exposed to $^{18}O_2$, only $C^{16}O^{18}O$ was observed as the CO oxidation product. The lack of involvement of lattice oxygen is further supported by the work of Chen and Goodman[47] who demonstrated high CO oxidation activity by titania covered with an ultrathin gold film.

Some research has suggested the active site for CO oxidation occurs at the gold-support interface.[48, 49] However, Chen concluded that since the titania support was not accessible to the CO, the active site must be on the gold and the role of the support is likely electronic in nature.[47]

Since the high activity of TiO_2 as a photocatalyst in the decomposition of DMMP is a result of the formation of the superoxide and gold nanoparticles were capable of forming this species without UV irradiation, it would follow that the Au/TiO_2 system would be capable of catalytic decomposition of DMMP in the dark. Panayotov and Morris examined this possibility and determined that Au nanoparticles supported on TiO_2 could oxidize DMMP at ambient temperatures in the dark.[17] The uptake of DMMP on Au/ TiO_2 and pure TiO_2 was initially studied in the absence of oxygen at 295 K, with no significant differences being observed by infrared spectroscopy. Some hydrolysis is observed for both surfaces involving residual surface hydroxyl groups and open TiO_2 regions. However, strong IR absorption bands near 2100 cm^{-1} are observed for the Au/ TiO_2 surface while no such absorption occurs in this region for pure TiO_2. This absorption is consistent with that of adsorbed CO and is indicative of DMMP oxidation.[17, 30] By analyzing variances in the adsorbed CO vibrational frequencies, Panayotov and Morris established the presence of oxidized gold and coordinatively unsaturated Ti^{+4} sites at the Au/ TiO_2 interface but not the TiO_2 surface. The difference in frequencies indicates that the gold nanoparticles promote the extraction of lattice oxygen, which is then involved in the oxidation of DMMP. Under anaerobic conditions, this process continues until the lattice oxygen is exhausted and DMMP oxidation slows. However, the Au/ TiO_2 surface can be regenerated simply by exposing the surface to oxygen, even at pressures as low as 0.01 Torr. This phenomenon is not observed with pure TiO_2 even after exposure to much higher concentrations of oxygen. Observing the ν_{co} absorption bands further elucidates the role of Au nanoparticles in

increasing the oxidative ability of the catalyst. When a DMMP covered Au/ TiO_2 surface is exposed to low levels of oxygen, a progressive conversion of $Au^{\delta+}$-CO (2130 cm^{-1}) to Au^{+}-CO (2170 cm^{-1}) is observed (Figure 1.8).

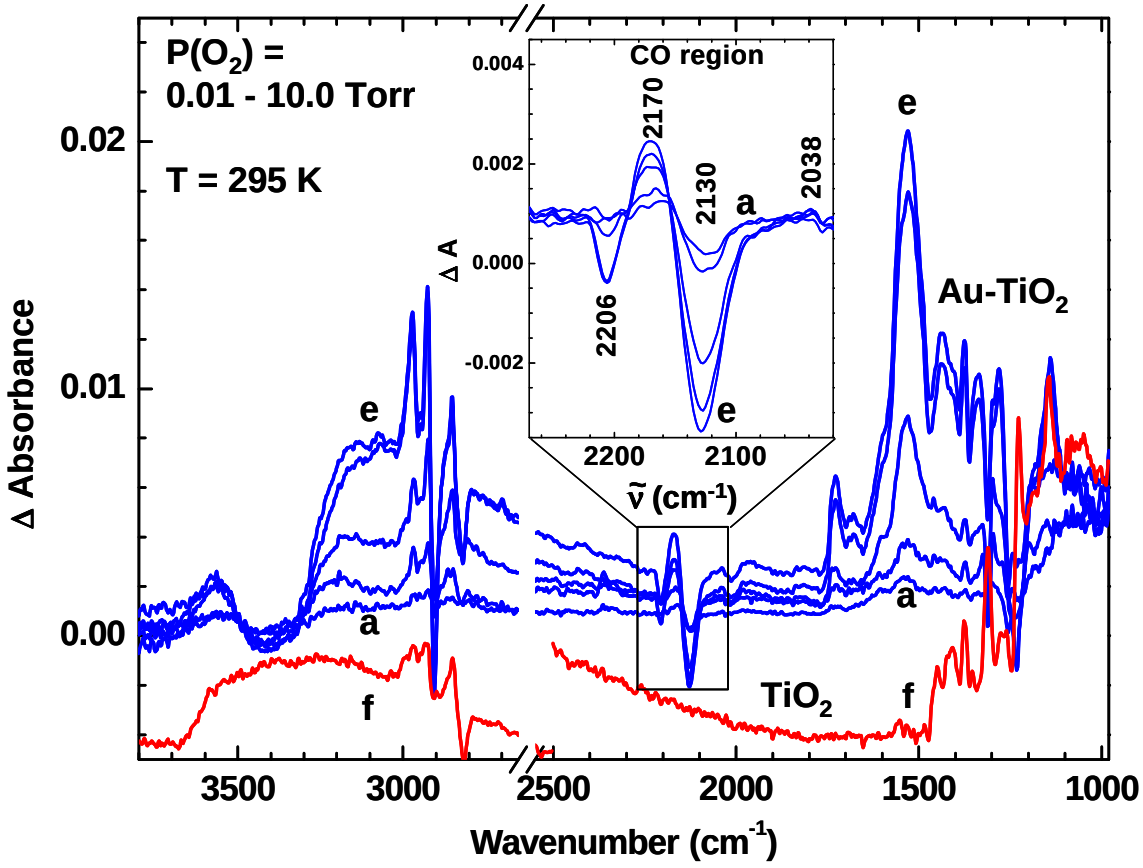

Figure 1.8: Difference spectra showing the evolution of Au^{+}(2170 cm^{-1}) and the depletion of $Au^{\delta+}$ (2130 cm^{-1}) by monitoring ν_{co}.[17]

The formation of cationic gold is a result of electron transfer from the partially positive gold to molecular oxygen to form the reactive superoxide as discussed previously. The extraction of lattice oxygen for the production of the superoxide is also observed by similar methods. As lattice oxygen is extracted, coordinatively unsaturated Ti^{+4} sites are formed. These sites adsorb the CO that is formed from the oxidation of DMMP and result in an increase in the Ti^{+4}CO

absorption band. Exposure to molecular oxygen also replenishes oxygen vacancies in the lattice, completing the catalytic cycle.

The aforementioned study describes a new class of highly reactive sorbents for organophosphates. Gold nanoparticles supported on titania are effective catalysts for the room temperature decomposition of DMMP without UV irradiation, a feat not achieved by previously discovered surfaces. Furthermore, the mechanism by which this catalytic activity is achieved has been elucidated. However, given the vast permutations of nanoparticle size, material, and support, the variables affecting the catalytic decomposition of organophosphates must be explored.

1.4 Objectives and Approach

The goal of the work described in this thesis is to **design and construct a high-throughput high vacuum instrument to investigate the ability of nanoparticulate transition metal-metal oxide surfaces to decompose chemical warfare agent simulants.** The instrument uses several analytical techniques to probe the activity of nanoparticulate systems. Infrared spectroscopy can monitor surface-bound species over time, temperature ranges, and simulant dosing. A differentially pumped mass spectrometer enables TPD studies and the ability to monitor desorbed decomposition products. A custom-designed doser provides the ability to apply a controlled flux of a simulant or other gas to the surface. These techniques can be used individually or simultaneously to perform a variety of experiments and investigate many aspects of gas-surface interactions.

To minimize background interference and prevent contamination of the surface, experiments are performed under vacuum conditions. Typically, ultrahigh vacuum conditions

($\leq 10^{-9}$ torr) are required to keep the surface clean over the timescale of the experiment. However, nanoparticles have a higher surface area than a flat sample but the flux of impinging gasses experienced by the surface remains the same. Due to the increased surface area, the time required for a nanoparticulate surface to be significantly contaminated at a certain pressure is increased by several orders of magnitude. Using nanoparticulate surfaces, we are able to keep the surface clean for a sufficiently long time to perform experiments in a high vacuum. Operating at high vacuum instead of ultrahigh vacuum conditions greatly reduces the amount of time needed to achieve an adequate vacuum after venting the chamber to change samples.

The instrument discussed in this work was designed to perform experiments that employ a combination of IR and mass spectrometry (MS) techniques to investigate gas-surface interactions. Figure 1.9 depicts a general experimental approach used to study interactions between CWA simulants and nanoparticles. Infrared spectroscopy is used to observe the surface, as well as species adsorbed to the surface. Mass spectrometry allows for the detection and identification of gas molecules that have desorbed from the surface. A custom-designed doser exposes the sample to a controlled flux of gas. Thermal control of the sample enables *in vacuo* cleaning of the surface and thermal desorption experiments. By combining infrared and mass spectrometric techniques and operating at high vacuum, we are able to perform a thorough investigation of gas-surface interactions with a high sample throughput.

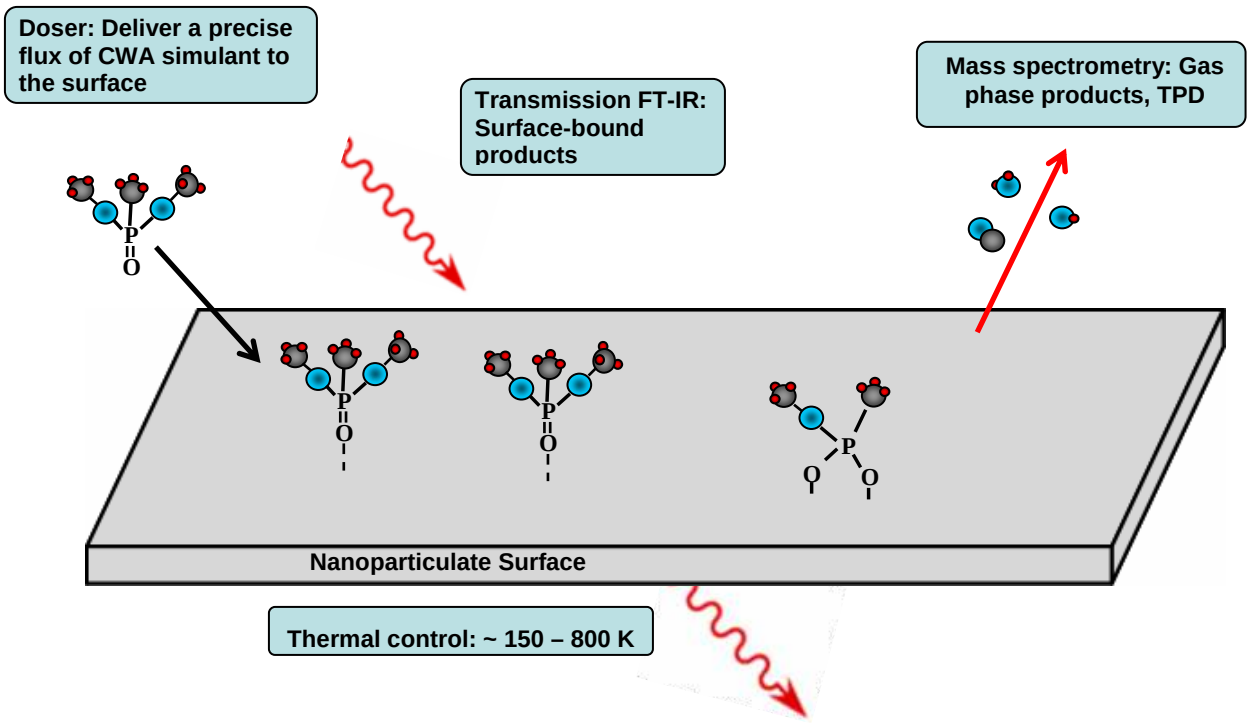

Figure 1.9: A drawing outlining our basic experimental approach depicting DMMP sticking to and reacting with the surface. IR spectroscopy is used to observe the surface and adsorbed species. The mass spectrometer detects molecules that desorb from the surface.

1.5 Summary

The threat of a CWA attack and the deficiencies of current decontamination methods underscore the need for further research of solid-state decontamination measures. Nanoparticulate metal oxide and metal oxide-supported nanoparticles represent a large class of materials with possible applications in CWA defense. The abundance of variables affecting the ability of metal oxide nanoparticles to sorb and decompose CWAs results in a vast number of potential CWA decontaminants. By constructing a high-throughput instrument that utilizes the techniques mentioned above, we hope to advance the understanding of the chemistry governing

interactions between CWA simulants and metal oxide nanoparticles. In addition to identifying nanoparticulate materials with a high activity towards the decomposition of CWA simulants, we intend to develop a more thorough fundamental understanding of CWA simulant-surface interactions to facilitate future studies or predictions regarding the behavior of real CWAs on surfaces.

Chapter 2 – Instrument Design and Construction

2.1 Introduction

Fourier-transform infrared spectroscopy (FT-IR) and mass spectrometry (MS) are powerful analytical techniques that can be used individually or simultaneously to provide extensive information about the interactions between a surface and adsorbed species. FT-IR can identify and quantify surface-bound species as well as the surface site to which they are bound. MS is capable of identifying and quantifying species that have desorbed from the surface. These techniques enable an array of studies to be conducted regarding the uptake and oxidative or hydrolytic decomposition of gases on surfaces. Frequently, techniques such as X-ray photoelectron spectroscopy (XPS) or precision dosing are employed in concert with FT-IR and MS to answer questions about gas-surface reactions. Altering the physical environment of the surface (such as temperature or exposure to light) may also provide data relevant to understanding a gas-surface interaction. Temperature programmed desorption (TPD) experiments can provide information about the binding energy of an adsorbate and are conducted by heating a sample in a controlled manner while detecting the desorbed molecules with a mass spectrometer. Various techniques can be combined to provide a great deal of information about the interactions between a gas and a surface, such as chemical warfare agent (CWA) simulants and metal oxide nanoparticles.

Several ultrahigh vacuum chambers have been constructed by members of our research group and are capable of performing experiments that explore the interactions between metal oxides and chemical warfare agent simulants. The instruments possess an extensive suite of analytical techniques including IR, MS, XPS, quartz crystal microbalance (QCM), and multi-gas dosing. In addition, the systems are designed so that the chamber that houses the sample can

reach pressures in the ultrahigh vacuum range. The array of instrumentation and low base pressure enable an extensive variety of experiments to be performed, allowing for in-depth studies of surfaces. However, ultrahigh vacuum instruments are not well-suited for high sample-throughput due to the time and difficulty associated with introducing a new sample. In some cases, operating the instrumentation can also be quite complex. Furthermore, these vacuum instruments have a large laboratory footprint, are relatively expensive, and require many months to design and construct. Although powerful investigative tools, ultrahigh vacuum instruments are not conducive to higher throughput studies.

Given the challenges associated with working with large, ultrahigh vacuum instruments, it was evident that a smaller, less complex vacuum instrument would be a valuable tool for high-throughput studies of nanoparticulate surfaces. By sacrificing several less relevant capabilities of the ultrahigh vacuum instruments while maintaining the functionality necessary for preliminary studies of a variety of surfaces, the operation of a vacuum instrument could be streamlined. A new instrument was designed that was, in comparison to the larger chambers in our laboratory, an order of magnitude cheaper, easier to operate and change samples, and relatively easy to construct. The small scale of the chamber also provides an instrument capable of fitting within a standard fume hood, enabling a safe method of performing high vacuum experiments with actual CWAs. Although using live agents is beyond the scope of work at Virginia Tech, current collaborations of our research group with the United States Army at the Edgewood Chemical Biological Center (ECBC) could greatly benefit from this capability. Recent efforts to design and construct a full-scale vacuum instrument are challenged by the complexity of the design, as well as the engineering of safeguards to mitigate hazards and concerns associated with operating with CWAs outside of a hood. The preparation of associated

standard operating procedures (SOPs) required for operation of the chamber using live agent outside of a fume hood is a complex and time consuming task. Since the entire instrument that is discussed in this work, with minor modifications, fits within a fume hood at ECBC, the execution of experiments with CWAs in a safe manner could be greatly expedited.

2.2 Instrument Design

2.2.1 Experimental Approach

The general experimental approach involves the use of infrared spectroscopy and mass spectrometry to observe the behavior of a surface. The surface is cooled, dosed with a gas, and then heated to desorb the gas. Infrared spectroscopy measures the infrared absorbance of the surface, an adsorbate, and the bonds between the two, providing quantitative and qualitative data regarding the surface and any adsorbed species. Mass spectrometry is used to detect and identify species that have desorbed from the surface. Sample cooling is used in conjunction with dosing to get the gas to stick to the surface while heating the sample can cause desorption of adsorbed particles. If the sample is heated linearly over a certain temperature range the desorption rate can provide valuable information, such as the activation energy for desorption of the adsorbate. The rate of desorption can be measured using MS or, less commonly, IR. We intend to apply this experimental approach to investigate the interactions between CWA simulants and nanoparticulate surfaces.

2.2.2 Vacuum Conditions Prevent Interference and Surface Contamination

Perhaps the most important consideration for the construction of an instrument capable of completing studies of gas-surface interactions is the pressure required to achieve high-quality results. In infrared studies, atmospheric gases and moisture can absorb energy from the IR beam

and cause significant interference. While there is no definitive pressure required for IR studies, as the pressure decreases, the sensitivity is increased and the occlusion of peaks due to infrared absorbance of gasses such as carbon dioxide and water can be minimized or eliminated. Mass spectrometric studies also necessitate operating under vacuum to eliminate interference from background gasses. The ionizer filament of the MS must also be kept under vacuum so that it does not burn out. In TPD experiments, the surface is heated and desorbed molecules are detected by the MS. A vacuum is necessary to ensure that the desorbed molecules reach the ionizer before their path is altered by a collision with another molecule. The pressure required to avoid such collisions depends on the distance the molecules must travel to reach the ionizer and the mean free path of the molecules in the chamber. The mean free path, λ, or the distance between collisions, is given by equation 2.1, where ξ is the diameter of the molecule and *n* is the number density of molecules.[50] These experiments are typically performed at the lowest pressures possible for a given system to minimize interferences and obtain the best possible data.

$$\lambda = \left(\frac{1}{\sqrt{2} n \pi \xi^2} \right) \tag{2.1}$$

An approximation of the pressure required for O_2 or N_2 ($\xi \approx 3\text{x}10^{-10}$ m) to travel the 10 cm from the surface to the mass spectrometer's ionizer results in a modest vacuum of $5\text{x}10^{-4}$ torr.

Surface contamination is a particularly important consideration for the proposed studies. When molecules are in the gas phase, they collide with each other, as well as surfaces. As the pressure increases, the number of collisions increases. The rate of these collisions with a surface is given by equation 2.2, where *Z* is the number of collisions and $\bar{v}$ is the average velocity deduced from the Maxwell-Boltzmann velocity distribution law, shown by equation 2.3, where *k* is the Boltzmann constant, *T* is temperature, and *m* is the molecular mass of the gas.

$$Z_{surface} = \frac{n\bar{v}}{4} (s^{-1}\ cm^{-2}) \tag{2.2}$$

$$\bar{v} = \left(\frac{8kT}{\pi m}\right)^{1/2} \tag{2.3}$$

The probability that molecules and atoms will chemically adsorb to the surface is known as the sticking probability and on a clean surface ranges from 0.1 to 1.0 for most molecules in air. Given a molecule diameter of $3x10^{-10}$ m (approximating the diameter for N_2 or O_2) and a sticking probability of 1.0, the time required to form a monolayer, t_m, on a clean, flat surface at 20°C is shown by equation 2.4.

$$t_m = \frac{2.5\times10^{-6}}{P(Torr)} \tag{2.4}$$

where P is the pressure in torr. As a result, the time it would take to form a monolayer at 760 torr is $3.3x10^{-9}$ s and thus a vacuum is required to keep the surface uncontaminated throughout the timescale of the experiment. The pressure required depends on the necessary timescale of the experiment and the time for monolayer formation at the lower limit of various pressure ranges is shown in Table 2.1.[50]

Table 2.1: Data for air at 20° C, assuming a flat surface, sticking probability of 1 and a molecular diameter of $3x10^{-10}$ m.[50]

	Pressure (torr)	Number Density (cm^{-3})	Mean Free Path (cm)	Surface Collision Frequency ($cm^{-2}\ s^{-1}$)	Time for Monolayer Formation (s)
Atmosphere	760	$2.7x10^{-19}$	$7x10^{-6}$	$3x10^{23}$	$3.3x10^{-9}$
Lower limit of:					
Rough Vacuum	10^{-3}	$3.5x10^{13}$	5	$4x10^{17}$	$2.5x10^{-3}$
High Vacuum	10^{-6}	$3.5x10^{10}$	$5x10^{3}$	$4x10^{14}$	2.5
Very High Vacuum	10^{-9}	$3.5x10^{7}$	$5x10^{6}$	$4x10^{11}$	$2.5x10^{3}$
Ultrahigh Vacuum	10^{-12}	$3.5x10^{4}$	$5x10^{9}$	$4x10^{8}$	$2.5x10^{6}$

As a result of interference from impinging molecules, ultrahigh vacuum (UHV, < $1x10^{-9}$ torr) conditions are needed to avoid significant contamination of a flat surface; however the proposed research deals with nanoparticulate surfaces. Although surface contamination is still a significant concern for nanoparticulate samples, the far greater number of active surface sites eases the conditions required to keep the surface significantly clean. For instance, a circular sample with a flat surface and a diameter of 7 mm would have a surface area of $1.5x10^{-4}$ m^2. At $1x10^{-6}$ torr, a monolayer would form after 2.5 seconds, completely covering the surface. If a similar, 7 mm diameter sample were prepared with nanoparticles, the surface area would be greatly increased. Degussa P25 is a commonly used, commercially available titania nanoparticle with a surface area of 50 m^2/g. If 300 mg of Degussa P25 nanoparticles were formed into a circular sample of the same diameter, the surface area would be 15 m^2 while the flux of gas colliding with the 7 mm spot would remain the same. This increases the monolayer formation time from 2.5 seconds to 250,000 seconds, which is more than enough time to carry out the planned experiments.

Adsorbed contaminants must be removed from the sample before experiments are performed. The nanoparticles and metal oxide supports are not prepared *in vacuo* so surface contamination occurs before the sample enters the chamber. As a result, the sample must be cleaned by heating under vacuum until the contaminants desorb. To clean the sample, the temperature of the surface must be significantly high and the pressure significantly low so that surface contaminants desorb, or more accurately, the rate of desorption must be greater than the rate of adsorption (including readsorption of desorbed molecules).

The motivation behind the construction of this instrument was to exploit the ability to operate at pressures above UHV. By constructing a small chamber and operating at a modest base pressure, the introduction of samples into the chamber is streamlined and the required pump-down time is relatively low. By taking these advantages into consideration in the design of both the instrument and procedures, the performance of a high-throughput instrument capable of effectively screening a wide variety of metal oxide-supported transition metal nanoparticles was optimized.

2.2.3 Design Overview

I designed and constructed a high vacuum instrument to study interactions between CWA simulants and nanoparticulate surfaces. The instrument's primary analytical techniques are FT-IR and MS. Sample heating and cooling allows for dosing and TPD studies. By developing a high throughput instrument that uses such techniques, we hope to advance the understanding of interactions between many CWA simulant/nanoparticle systems.

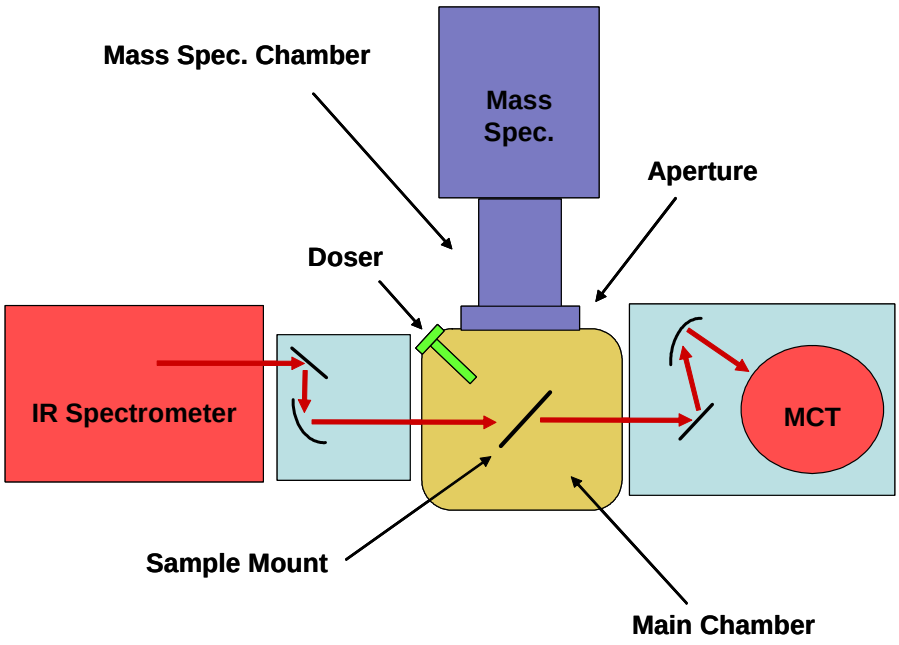

Figure 2.1: A top-down view depicting the basic arrangement of the instrument. Vacuum pumps (not visible) are located beneath each chamber.

The orientation of components was determined by a balance between the need for high vacuum and the requirement of performing infrared spectroscopy and mass spectrometry simultaneously on nanoparticulate samples. In transmission IR, the IR beam must pass through the chamber, intersecting the sample in the chamber as it proceeds to the detector. Optical mirrors in nitrogen-purged enclosures direct and focus the beam onto the sample, through the chamber, and onto the mercury cadmium telluride (MCT) detector. The sample must also be facing the mass spectrometer's ionizer so that the desorbed molecules have a direct line of flight to the ionizer. To accomplish this, the IR beam is in a transverse orientation relative to the mass spectrometer and the sample is maintained so that the face of the sample is 45° from normal to the IR beam path and mass spectrometer. A secondary chamber, which houses the mass spectrometer, is separated from the main chamber by an aperture to decrease interference from

non-target gas molecules. The mass spectrometer chamber is differentially pumped to increase the operating pressure of the main chamber while maintaining a sufficiently low pressure to operate the MS. The orientation of the chamber and its components, depicted in Figure 2.1, was chosen to provide a functional and compact design.

2.2.4 Design Considerations:

Although a small vacuum chamber might have decreased functionality in terms of the ability to connect a large array of instruments, a small chamber can provide several advantages over a larger one. For a given vacuum pump, the pumpdown time and base pressure decrease with chamber size. The pumpdown time, *t*, can be calculated by equation 2.5 where *V* is the volume of the chamber, *S* is the pumping speed, P_0 is the starting pressure, and *P* is the final pressure of the chamber.

$$t = \frac{V}{S} \ln\left(\frac{P_0}{P}\right) \tag{2.5}$$

This calculation assumes a constant pumping speed and does not account for outgassing or leaks. A material such as stainless steel that has been exposed to atmosphere may outgas at a rate of 10^{-8} torr·liter·s^{-1} for every square cm of the interior wall of the chamber.[50] It follows that maximizing pumping speed while minimizing the interior surface area of the chamber will result in a lower base pressure. An adequate base pressure and reasonable pumping speed can be maintained by smaller pumps, thereby decreasing the size and cost of the instrument.

Another consideration allowing smaller, less expensive pumps to be used while maintaining a low base pressure in the chamber is the fraction of the interior surface area of the chamber that is taken up by the pump. At low pressures where the mean free path is long in relation to the interior dimensions of the chamber, molecules collide primarily with the chamber walls, not other molecules. In this pressure regime pumps no longer “pump” by creating a

pressure gradient but instead remove only molecules that come into contact with the face of the pump via their flight path. By maximizing the percentage of internal surface area of the chamber that is taken up by the face of the pumps, the likelihood a molecule will collide with the pump is also maximized, resulting in a lower base pressure.[51]

Connections capable of maintaining a vacuum must be made between the chamber and other components and are formed using Conflat® flanges. A flat oxygen free high conductivity (OFHC) copper gasket is seated between two flanges and as they are tightened, a conical sealing edge on each of the flanges, also known as a knife edge, bites into the gasket resulting in a seal that is vacuum tight to pressures in the range of $1x10^{-13}$ torr.[52] The highly effective seal, combined with ease of use and functionality over a wide range of temperatures (−200 – 450 °C) makes it a staple in UHV work.

2.2.5 Vacuum Chambers and Pumps

A compact yet highly functionalized chamber was selected as the main chamber for the instrument, providing the necessary connectivity for the IR windows, pumps, sample mount, doser, and MS chamber. Differential pumping is achieved by separating the main chamber and mass spectrometer chamber with an aperture and pumping each chamber independently. This arrangement decreases the background signal in the mass spectrum and allows the mass spectrometer to be operated while dosing at higher pressures in the main chamber. Turbomolecular/molecular drag hybrid pumps backed by diaphragm pumps were selected to provide the vacuum in both chambers. Due to the small volume of the chambers and the efficacy of the pumps, a sufficiently high vacuum is provided by the relatively small and inexpensive turbo/drag pumping stations.

Main Chamber - An expanded spherical cube from Kimball Physics Inc. (MCF275-ESC608) was selected as the main chamber for the instrument (Figure 2.2). Its design consists of a hollow sphere that has ports for flange connections cut in cubical symmetry. It is machined out of a single billet of stainless steel that eliminates the need for welds. Welding for vacuum applications can be expensive and requires a highly specialized technique to ensure a weld does not outgas or leak when exposed to high vacuum conditions. While larger chambers may not be cheaper to machine out of a single piece of metal (the volume of the billet needed for a cubic chamber increases by length cubed and with it the amount of material that is to be machined out), small, highly-functionalized monolithic chambers are significantly less expensive due to these factors. A variety of chamber sizes are available "off the shelf" which results in a lower price than custom design and fabrication. The chamber has six 2.75" Conflat flanges on the faces of the cube, and eight 1.33" Conflat flanges cut into each of the vertices. The result is a compact design with a minimal sacrifice in connectivity. Despite its small size, the spherical cube provides a sufficient internal volume and workable space to hold the sample mount and not impede the IR path or flight of desorbed molecules from the sample surface to the mass spectrometer.

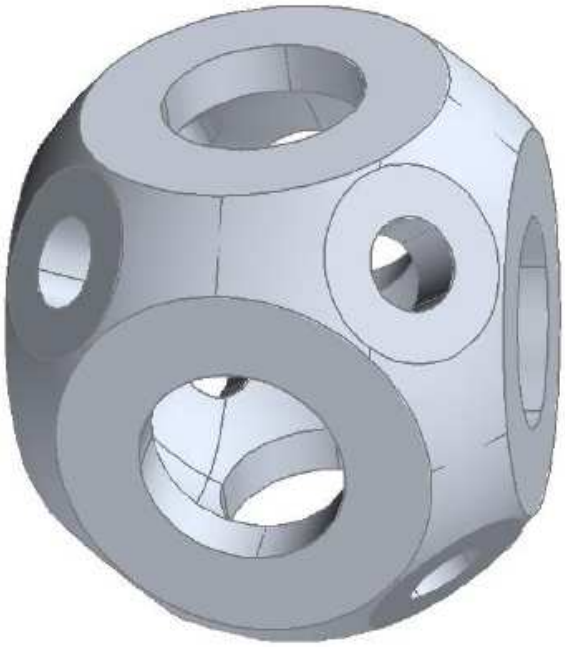

Figure 2.2: A drawing of the main chamber. The chamber is a hollow sphere with six 2.75" and eight 1.33" Conflat flange connections providing high connectivity and a compact design.

The chamber and attached components were arranged to provide a configuration conducive to the operation and physical support of the components. The beam path of the IR passes through 2.75" flanges on opposing sides of the chamber in a horizontal orientation and an aperture and second chamber is attached perpendicular to the IR beam path, also in a horizontal orientation. The path to the MS ionizer and the IR beam path intersect in the center of the main chamber so both methods can be used to analyze a sample simultaneously. The top flange connects to the support for the sample mount while the bottom flange connects to a turbomolecular pump. While the spatial orientation of these components is not critical to their functionality, some of the later design considerations are contingent upon this orientation. The

layout was chosen to provide the easiest path of construction while resulting in a compact design with easy access to adjustable components.

Mass Spectrometry Chamber - A standard cross with 2.75" Conflat flanges was chosen as the chamber to house the mass spectrometer. The low cost and availability made it an ideal choice and the standard dimensions allow for an expansion of the chamber to be carried out simply by replacing the chamber with a 5- or 6-way cross. The low internal volume of the cross aids in pumping speed while allowing for connections to the main chamber, pump, mass spectrometer, and a pressure gauge. The pressure gauge is a Pfeiffer PKR 251 FullRange™ gauge (p/n: PTR26002) that can measure pressures from $4x10^{-9}$ to 750 torr and consists of a Pirani gauge and a cold cathode gauge in a single housing. Pressures from $4x10^{-9}$ to around $1x10^{-3}$ torr are measured by the cold cathode portion of the gauge and pressures up to 750 torr are measured by the Pirani gauge.[53] The pressure gauge allows monitoring of the mass spectrometry chamber pressure that enables the approximation of the pressure in the main chamber and flux of a gas flowing into the chamber while dosing. In addition, by knowing the pressure of the mass spectrometry chamber (and thus the pressure at the mass spectrometer's ionizer filament) we can make sure the mass spectrometer is turned on and operated only in sufficiently low pressure so as not to burn out the filament or electron multiplier.

Aperture - To decrease the background signal in the mass spectra, an aperture was placed between the MS chamber and the main chamber. The aperture limits the open area connecting the chambers and deflects most of the gasses that have desorbed from the chamber walls, sample mount, or grid back into the main chamber. The hole of the aperture was placed directly between the sample and the MS, providing line-of-sight detection of the sample. Molecules that have desorbed from the sample pass through the aperture and are ionized and

detected by the mass spectrometer. The size of the aperture was calculated to maximize the number of target molecules that reach the ionizer and minimize the number of errant molecules that are detected. By treating the mass spectrometer's ionizer and entrance to the quadrupole rods as a single point at the ionizer filament and using the diameter of the sample spot, the diameter of the aperture was calculated.

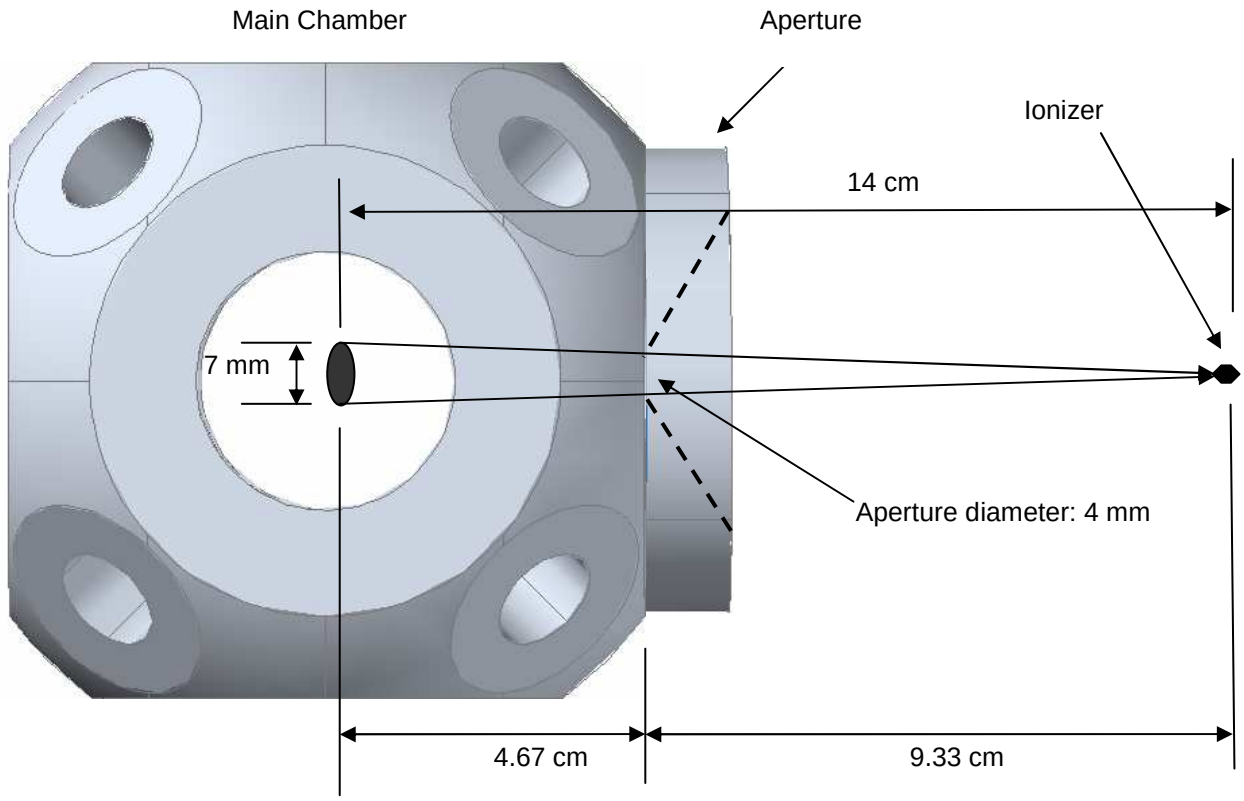

Figure 2.3: Determining the aperture size. Not drawn to scale.

Differential pumping of the chambers enables the MS to be operated while the pressure in the main chamber is outside the operable range for the MS. While dosing a sample, the pressure in the main chamber increases due to the introduction of gas. The gas that does not stick to the sample is either pumped away in the main chamber or moves into the MS chamber. The aperture

limits the throughput of gas from the main chamber, allowing the MS chamber to be maintained at a lower pressure. This means that the pressure at the MS ionizer can remain within the operating range even if the pressure in the main chamber is too high.

If the length of the aperture (the distance a molecule must travel to pass through the aperture) is sufficiently close to zero, the transmission probability of target molecules is maximized and the conductance is maximized. The conductance of the aperture for a gas in the molecular flow regime through a tube with an opening of area *A* is given by equation 2.6 where *a* is the transmission probability.

$$C = \frac{1}{4} vAa \tag{2.6}$$

Also known as the Clausing factor, the value of *a* is not simple to evaluate but can be approximated by referencing tables for a given length/diameter ratio of a tube (or aperture). When the length (or more accurately length/diameter ratio) of this tube approaches zero, the transmission probability approaches unity and can be ignored. Reducing the aperture length increases the conductance of target molecules while still preventing non-target molecules from entering the mass spectrometry chamber. Also, by sufficiently reducing the length of the aperture, the conductance of the aperture becomes simpler to evaluate. As the length of the aperture approaches zero, the calculation for the conductance of the aperture is simplified by eliminating the transmission probability factor to give equation 2.7.[54-56]

$$C = \frac{1}{4} vA \tag{2.7}$$

The throughput, *Q*, of the aperture is calculated as the product of the conductance and the pressure, *P*, on either side of the aperture such that

$$Q_{P_1 \to P_2} = CP_1 - CP_2 \tag{2.8}$$

Ignoring factors such as leaks and outgassing, the throughput of the aperture is equal to the throughput of the pump on the mass spectrometry chamber. Since pumping speed and the pressure in the mass spectrometry chamber are known, equation 2.8 can be used to determine the pressure inside the main chamber.

The necessity of the diameter of the aperture to be accurately known at a point with a minimal thickness presented a challenge to the design and fabrication of the aperture.

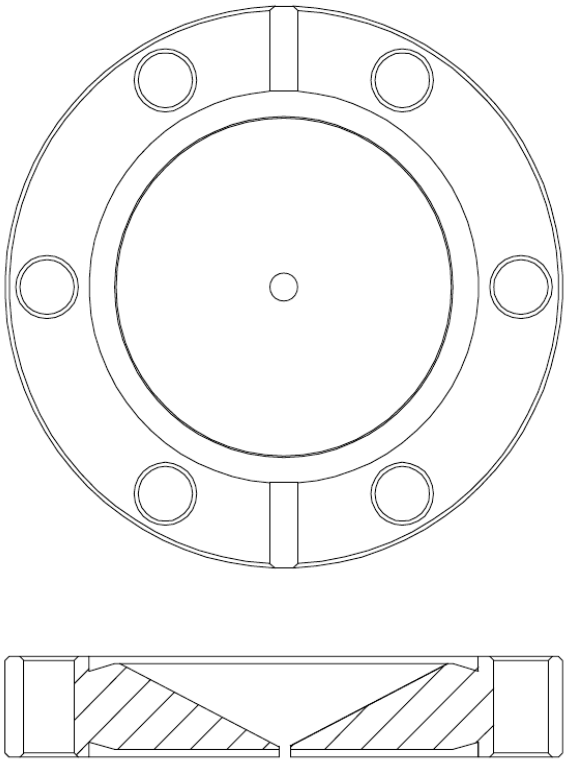

Figure 2.4: Top and side view drawings of the aperture. The conical shape provides a sturdy, easily-constructed aperture with a minimum length between the conic and flat sides.

To avoid limiting the flow of molecules desorbed from the sample, the optimal length of the aperture is zero, thereby minimizing the limiting effect that length has on the conductance, as seen in equation 2.6. Machining a flat portion of the flange to a thickness approaching zero would result in a structurally weak portion surrounding the hole of the aperture. Removing a conic section from both sides of the flange would result in a sufficiently sturdy part, however extremely high precision would be required by the machinist to ensure the hole diameter was accurately known. The removal a single conic section results in an easily machineable, robust aperture with a maximum conductance. An aperture of this design was constructed by drilling a 4mm hole in a double-sided 2.75" blank flange and removing material with a mill to form the conic section. The custom aperture is depicted in Figure 2.4 and provides a sturdy part with an accurately known hole diameter that was constructed for not much more than the cost of a standard blank flange (Dillon & Dillon Machining, Inc., Custom Part).

Vacuum Pumps - To achieve a vacuum, the air within the chamber must be removed by a vacuum pump. As mentioned prior, both chambers must be capable reaching pressures in the high or ultrahigh vacuum range. The evacuation of the instrument is achieved by a Pfeiffer Vacuum turbomolecular/drag pump connected to each chamber. A turbo/drag pump is a hybrid of a turbomolecular pump and a molecular drag pump. While turbomolecular pumps are capable of higher pumping speeds, they must be operated in conjunction with a backing pump that is capable of maintaining a foreline pressure of about 0.1 torr. Molecular drag pumps are not capable of achieving the same pumping speeds as a similar turbomolecular pump but can operate at much higher foreline pressures, enabling the use of inexpensive, oil-free backing pumps. Hybrid turbo/drag pumps use a combination of the two designs to provide a faster pumping speed than molecular drag pumps while being able to operate at relatively high foreline

pressures. Due in part to previously discussed design aspects of the instrument, a pressure sufficiently low to execute the planned experiments can easily be obtained by using turbo/drag pumps and diaphragm backing pumps, resulting in an oil-free system that minimizes overall size, weight, and cost. Pfeiffer HiPace 80 turbo/drag pumps were chosen as the two main pumps and are each capable of evacuating the chambers at a rate of 67 l/s. The pumps were purchased as a component of the Pfeiffer HiCube 80 pumping station that provides the controlling unit for the pump, a reader for a vacuum gauge, real-time monitoring of the pump operating parameters and a 15 l/minute diaphragm backing pump. The diaphragm pumps also serve as roughing pumps during the initial pumpdown of the chamber from atmospheric pressure. The housing for the control unit and diaphragm pump provides the support for the pumps, which in turn support the chambers and their attached equipment and instrumentation. Due to concerns regarding vibration, the diaphragm pumps were relocated from their original housing to a surface not in direct contact with the chambers. The pumping stations provide an inexpensive, quick, and effective method of achieving high vacuum conditions in the instrument.

2.2.6 - Sample Mount and Manipulator

A custom sample mount was designed for the instrument to provide thermal control of the sample, temperature feedback, and infrared transmission, as well as the ability to manipulate the sample within the chamber while under vacuum. While it may not seem to be an inherently difficult problem, mounting a nanoparticulate sample inside the chamber presents several challenges. The objective of this instrument is to study nanoparticles, which may have a granular to powdery composition, so the suspension of the sample in the middle of the chamber becomes a significant consideration. Manipulation of the sample is also crucial so that it is aligned with the IR beam path, the MS, and the doser. During a TPD experiment, the sample

must be heated to desorb molecules and cooled while dosing to encourage the adsorption of molecules. Controlling and monitoring the temperature of the sample is also very important in order to gather information regarding the interactions between the nanoparticles and the dosed simulant. The issue of sample mount design is further complicated by the need to maintain a high vacuum seal with the chamber.

Fortunately, a sample mount design using tungsten mesh as a support for particulate samples has already been described in the literature.[57] An instrument and sample mount of similar design described by Panayotov et al.[42] is presently in our laboratory and served as a starting point for the design of a new sample mount. The suspension of the particles is achieved by pressing them onto a piece of tungsten mesh. The mesh was purchased from Buckbee-Mears Co., and is fabricated by etching a pattern of 0.3 mm square holes in a sheet of tungsten metal, resulting in a screen-like material that has an IR transmittance of approximately 60-70%. A section of the mesh is cut to size and secured in a circular mold with a diameter of 7 mm. The nanoparticles are placed in the mold on top of the mesh and then compressed using a piston at 90,000 kPa for two minutes. This process can be repeated for a different spot on the same piece of mesh to apply multiple sample spots to the same mesh. In addition to providing a non-opaque medium to support the nanoparticles, the mesh is able to be resistively heated. Tungsten has a greater resistance than the copper to which it is secured and by applying a current to the mesh the temperature of the surface can be increased. The ability to heat the sample is crucial to running a TPD experiment as well as cleaning the surface under vacuum. For such applications, it is necessary to be able to monitor the temperature of the sample in real time. This is achieved by using a type K thermocouple. The thermocouple leads (chromel and alumel) are spot welded on the mesh to form a junction where a voltage difference occurs. The voltage difference varies as a

function of temperature. The thermocouple leads pass through a vacuum feedthrough and are connected to a thermocouple reader that converts the voltage difference to a temperature. In addition to real time monitoring of the sample temperature, the output of the thermocouple can be connected to a proportion-integral-derivative (PID) controller. This device can control the current used to heat the sample, thereby facilitating sample heating at a linear ramp rate, as required by TPD studies.

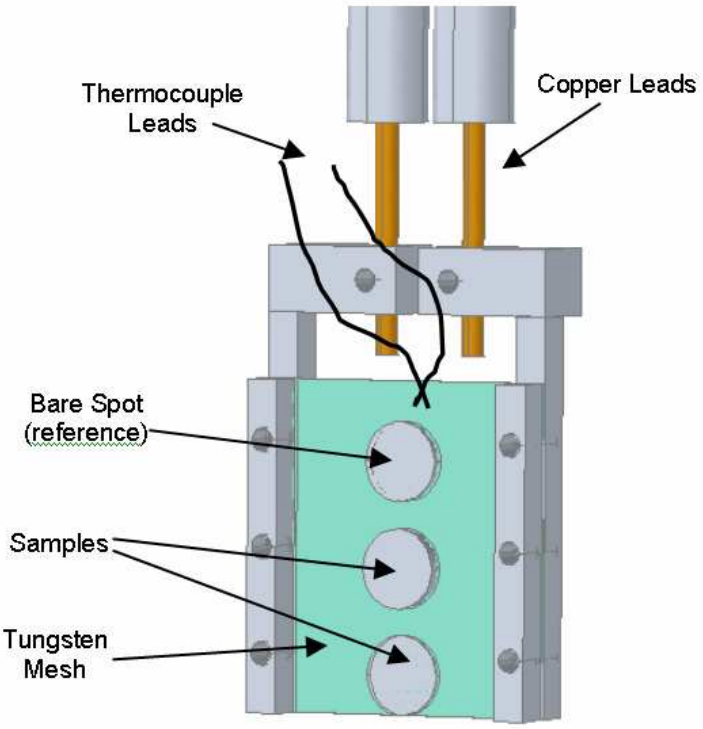

Figure 2.5: A depiction of the sample mount, tungsten mesh, thermocouple, and copper power leads.

A sample mount was designed and fabricated specifically for use in the instrument described in the present work. It is similar to the mount described by Panayotov et al. but several changes were made. The sample mount is used to hold the mesh in place and is shown in Figure 2.5. The mount was machined from a 0.25" thick sheet of oxygen-free high-conductivity

(OFHC) copper. Copper was chosen for its machinability and OFHC copper was used due to its low Ohmic resistance and low outgassing properties. As depicted in Figure 2.5, the mesh is held in place by compression provided when the front and back pieces are screwed together. This compression also provides the electrical contact for the heating current to flow from the copper to the tungsten mesh. The sample mount was designed to hold a piece of mesh large enough for two 7 mm sample spots and a bare mesh reference spot in a vertical orientation. As shown in Figure 2.6, the sample mount is attached to copper leads from the feedthrough, which are used to support the sample mount and provide the thermal and electrical conductivity for sample cooling and heating. The sample must be positioned in the chamber so that the surface of the sample is facing the IR beam path, as well as the aperture and mass spectrometer ionizer. This is achieved by rotating the mount so that the IR and MS paths intersect the sample at a 45° angle. In this orientation, the sample mount must be sufficiently low-profile so as not to block the IR beam or deflect desorbed molecules away from the aperture and MS. The copper leads from the feedthrough are offset from the center of the chamber. To limit the change of sample position in the "x" and "y" directions when the sample is rotated about the z-axis, the sample mount is designed to account for the offset of the leads. This ensures that the sample spots remain at the intersection of the IR beam path and the flight path for the mass spectrometer when the sample mount is rotated. The electrical current used to heat the tungsten mesh is carried to the sample mount by copper leads from a vacuum feedthrough. The power leads, as well as the thermocouple leads, are insulated from the body of the feedthrough using ceramic insulators, enabling the transmission of electrical current from atmosphere to vacuum. For the present application, a feedthrough on a 1.33" Conflat flange was used (Insulator Seal Inc, P9138941).

The sample mount and feedthrough are placed in the chamber through the top 2.75" flange of the main chamber. To utilize the multiple sample spots on the mesh, the sample mount must be able to be moved vertically while still under vacuum. Vertical translation of the sample mount is accomplished by a bellows-sealed linear translation stage connected to the top of the chamber via a 2.75" Conflat connection. The rotational alignment of the sample with respect to the IR path and MS must be adjustable; however rotation is not required while the sample is under vacuum. Also, a high or ultrahigh vacuum seal must be created that bridges the diameter difference of the 1.33" flange of the feedthrough and the 2.75" flange of the main chamber. To do this, the feedthrough was connected to the 1.33" flange of a half nipple. The weldable side of the half nipple was then welded to a 2.75" rotatable blank flange that had been bored out to accept the half nipple. The length of the half nipple was selected so that either of the sample spots or the bare mesh reference could be positioned at the proper height in the chamber to intersect with the IR beam and be in line-of-sight with the MS. A significant advantage to this design is the dewar that is formed by the vacuum insulation of the feedthrough and half nipple. This can act as a reservoir for liquid nitrogen or some other cold material, enabling the sample to be cooled conductively through the copper leads and sample mount. While sample cooling to 250 K has been achieved with the instrument by flowing cold nitrogen gas through the dewar, an almost identical setup constructed for another instrument has demonstrated sample cooling to 125 K using liquid nitrogen. The sample was also resistively heated to temperatures in excess of 700 K using alternating current and was controlled with a variable autotransformer. A manual temperature ramp during a TPD experiment has been carried out with the autotransformer and a PID has also been used to control the current and heat the sample in a linear ramp. Although some relatively simple machining was done to fabricate certain parts, the sample mount,

manipulator, and dewar were fashioned from commercially available metal stock or off-the-shelf parts, resulting in an inexpensive yet functional sample mount.

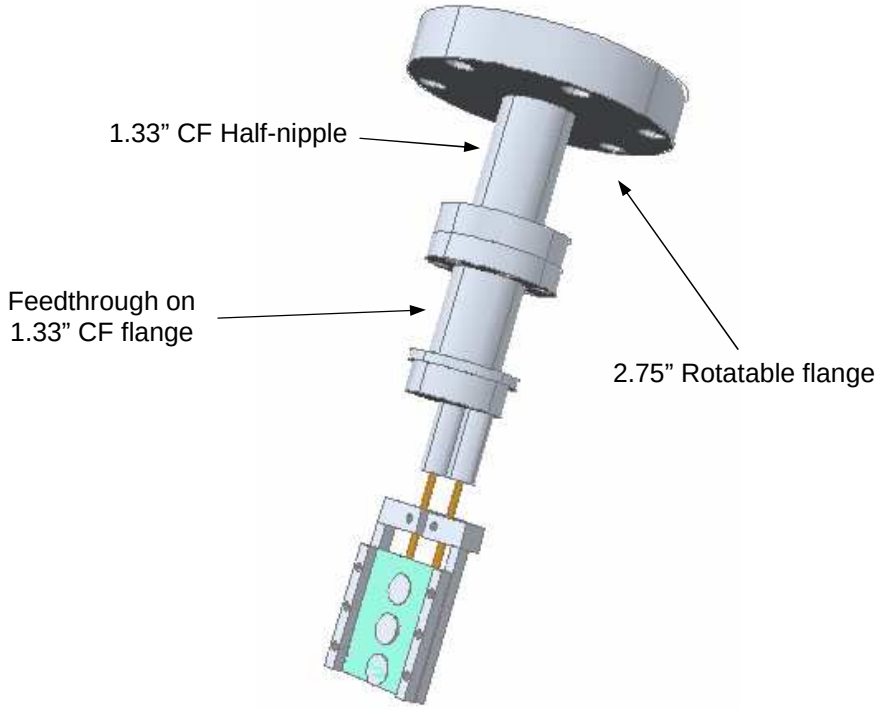

Figure 2.6: A depiction of the sample mount, feedthrough, and liquid nitrogen reservoir (thermocouple leads omitted). The sample mount is connected to the copper leads of the feedthrough, which provide electrical and thermal conductivity. The inside of the feedthrough and half-nipple forms the dewar. Liquid nitrogen or dry ice are added through a hole in the top of the 2.75” flange to provide sample cooling.

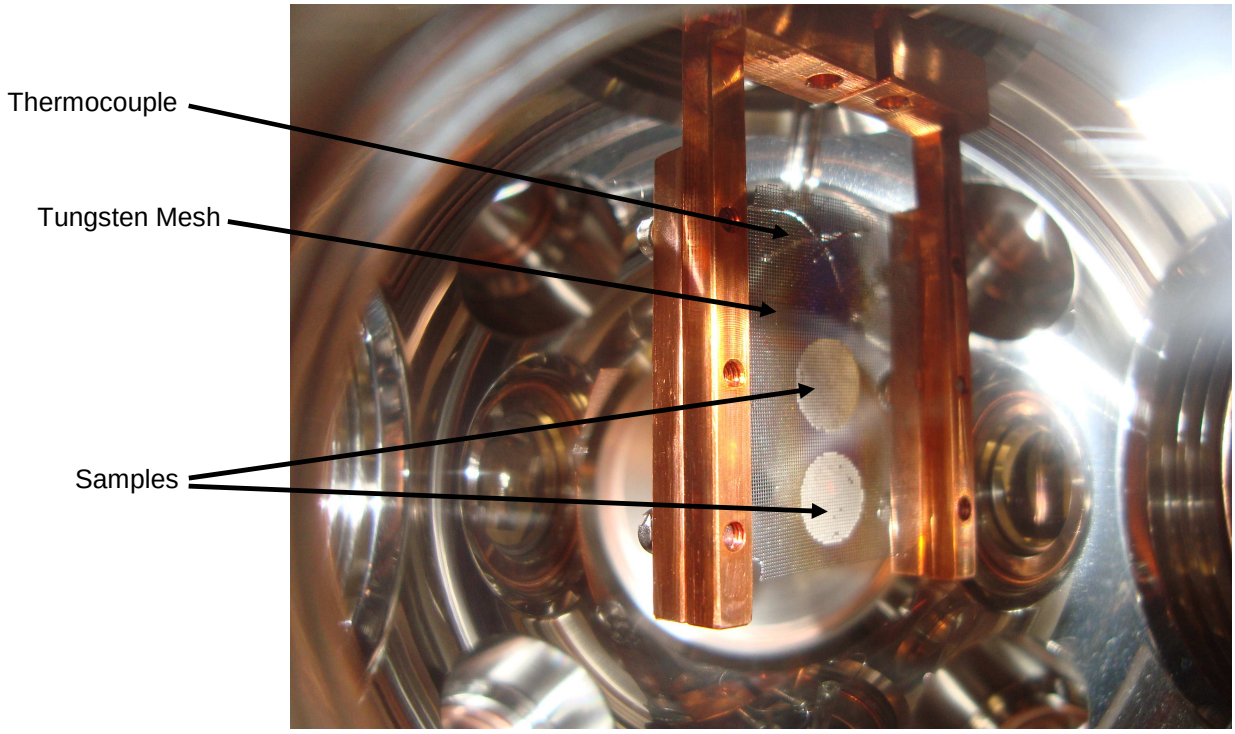

Figure 2.7: A picture showing the sample mount with mesh, thermocouple, and samples inside the chamber. The tungsten mesh supports the nanoparticulate samples while allowing infrared transmission. The IR beam proceeds from left to right in this picture and the aperture is partially visible behind the sample mount. A thermocouple spot-welded to the mesh provides temperature feedback.

2.2.7 - Residual Gas Analyzer

Mass spectrometry is a valuable tool for surface analysis, allowing for the quantification and identification of desorbed gasses, as well as TPD studies. TPD can be used to determine the amount and identity of species that desorb from the surface upon heating, as well as the energy of adsorption. By heating the surface at a controlled rate and plotting the pressure of a given mass to charge (m/z) ratio, valuable information can be gathered regarding surface kinetics. As a

result, a mass spectrometer is an excellent tool with which to study gas-surface reactions such as those between a CWA simulant and metal oxide nanoparticles.

Mass spectrometers can be large, heavy, expensive, and can require ultrahigh vacuum to operate. Consequently, they do not coincide with the design philosophy of this chamber. A residual gas analyzer (RGA), however, does provide the ability to run TPD experiments and detect and identify desorbed species with a minimal cost and size. RGAs are basically miniature quadrupole mass spectrometers and are typically robust and relatively inexpensive. A Stanford Research Systems Residual Gas Analyzer 300 was used for this application. The RGA is capable of detecting molecules with a mass to charge ratio of 1-300 amu. Dual thoriated iridium filaments ionize the molecules so that they can be mass separated by the quadrupole rods. The filaments in the RGA can be easily replaced if necessary. A Faraday cup allows the detection of species from $1x10^{-5}$ to $5x10^{-11}$ torr. This range is extended down to $5x10^{-14}$ torr with a multi-channel continuous-dynode electron multiplier. The resolution at 10% of the peak height is at least 0.5 amu. The electronic control unit can be removed, permitting the system to be baked out to 300°C. The RGA can be connected to and controlled by nearly any computer system with a standard RS-232 connection. While the RGA is small and inexpensive compared with mass spectrometers, the capabilities of the RGA meet those necessary for the experiments for which the instrument was designed.

2.2.8 – Infrared Spectrometer and Optics

Transmission Fourier-transform infrared (FT-IR) spectroscopy is a valuable technique for surface studies and can be used to monitor the reaction of adsorbates on surfaces. The absorbance of IR radiation as it passes through a sample can be used to identify chemical bonds in the sample material. Difference spectroscopy uses the spectrum of the sample as a

background, facilitating the observation of subtle changes in the system and allowing changes in adsorbed species to be detected. If decomposition of adsorbed molecules occurs, new peaks will emerge in the difference spectrum where the decomposition products absorb infrared energy. Subsequently, a decrease in absorbance is also observed where bonds were broken. Further information on the nature of the gas-surface bonding can be obtained by small shifts in the absorbance frequency. The change in frequency is caused by a change in the force constant, *k*, of the bond, and is approximated by equation 2.9 where ν is the vibrational frequency, and μ is the reduced mass[58].

$$\nu = \frac{1}{2\pi}\left(\frac{k}{\mu}\right)^{\frac{1}{2}} \tag{2.9}$$

A frequency shift would indicate that the surface is interacting with the adsorbed molecule and can provide information regarding which atoms interact with the surface and in what orientation the molecule is when it sticks to the surface. Information regarding the surface can be obtained by monitoring the IR absorption of different surface modes. IR spectroscopy is a powerful tool to observe gas-surface interactions and, as a result, was chosen as one of the main analytical techniques to investigate CWA simulants and nanoparticles.

The differences in the spectrum that occur as a result of changes on the surface of the sample are detectable by FT-IR spectroscopy; however, these changes might be occluded by the absorption spectrum of the sample itself, as well as the tungsten mesh. A background spectrum of the sample is collected prior to initiating the experiment. The background can be automatically subtracted by the software used to collect spectra and control the spectrometer. This process results in a spectrum that is easy to read and interpret. A flat line is observed if no change in the sample IR absorbance occurs. If the amount of an IR-active species on the surface

increases, a new peak (positive change in absorbance) is observed at the frequency where the adsorbed species absorbs IR radiation. As a corollary, the inverse behavior is true where a species desorbing from the surface would result in a negative value for change in absorbance. Using difference spectroscopy, changes in absorbance appear as deviations from a flat line, as opposed to subtle deviations in a spectrum dominated by the sample, facilitating the interpretation of the spectrum.

The infrared (IR) spectrometer used in this setup is a Nicolet Nexus 470 E.S.P. FT-IR spectrometer, capable of providing a spectral resolution of 0.125 cm^{-1} over the mid-IR region from 400-5000 cm^{-1}. The spectrometer is setup in a Michelson interferometer arrangement with a KBr beamsplitter and a Si-C globar source. The instrument is constantly purged with nitrogen to eliminate interference from IR-absorbing molecules present in air such as carbon dioxide and water vapor. A flat mirror directs the IR beam through an external port of the spectrometer housing and can be moved out of the beam path with an electric motor, allowing the internal compartment of the instrument to be used without interrupting the purge. This feature allows the internal compartment of the spectrometer to be used for other experiments. In keeping with the goals of this project to keep cost and laboratory footprint to a minimum, operability of both the internal compartment and the external port allow the same spectrometer to be used concurrently for different projects.

A nitrogen-purged enclosure eliminates interference from atmospheric gasses and is used to house mirrors that direct and focus the IR beam. The collimated beam leaving the external port of the spectrometer proceeds into a nitrogen-purged optics enclosure where a flat mirror directs the beam onto an elliptical focusing mirror, as shown in Figure 2.8. The focusing mirror was salvaged from a non-functional IR spectrometer and is positioned so that the focal length of

the mirror is equal to its distance from the sample, providing a spot diameter of approximately 20 μm. An adjustable platform within the enclosure allows the optics to be set at an appropriate height relative to the spectrometer. Fine adjustments to the beam path can be made in three dimensions via the mount for the flat mirror. By altering the beam path, the point where the beam encounters the sample can be changed. This allows for a quick and easy method of accounting for variances in the sample position after moving from sample to sample on the same mesh using the linear translator or after the sample mount is moved to attach a new mesh. The enclosure is constructed from 3/16" sheet poly(methyl methacrylate) and is continuously purged with nitrogen from the IR spectrometer. An extendable tube constructed from two pieces of concentric PVC pipe sealed with elastomer O-rings connects the purge flow from the spectrometer to the optics enclosure. The tube assembly is friction-fit in the spectrometer port with electrical tape and is sealed to the optics enclosure with weather stripping.

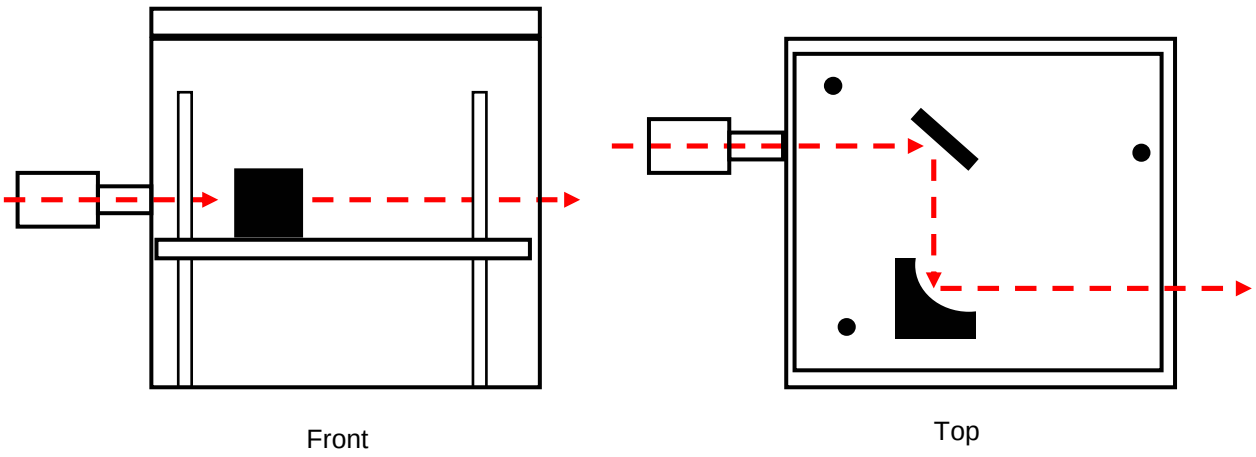

Figure 2.8: Front and top views of the focusing optics enclosure. The dashed line indicates IR beam path. A flat mirror directs the collimated IR beam towards an elliptical mirror that focuses the beam onto the sample. The mirrors are positioned at the proper height relative to the spectrometer by an adjustable platform.

As the IR beam leaves the chamber it enters another nitrogen-purged enclosure (Figure 2.9) that houses the detector and mirrors to direct and focus the beam on the detector. Inside the enclosure, the beam is reflected off a flat mirror onto a parabolic focusing mirror that directs the beam towards the detector. The flat mirror is on an adjustable mount and is used for alignment of the beam with the detector. The mirrors and mirror mounts were salvaged from other optics setups in our laboratory that were not in use. The detector is a liquid nitrogen-cooled mercury-cadmium-telluride A (MCT-A) detector purchased from Thermo Electron North America, LLC (840-070200) with a cadmium telluride window. The greater sensitivity of the MCT-A is an obvious advantage over the MCT-B and any benefit of the greater spectral range of the MCT-B at lower energy is nullified due to interference from IR-active phonons from the sample. The enclosure was constructed by former research group member Gregory Sincek for use on a different instrument but was modified for use with the instrument discussed in this work. It is constructed from 1/4" plate aluminum and rests on top of four bolts secured to an aluminum platform. The bolts provide a simple, adjustable support to position the box at the appropriate height in relation to the IR beam. A poly(methyl methacrylate) lid was constructed for the box and a small hole in the lid above the detector provides access to fill the liquid nitrogen reservoir in the detector without interrupting the purge, allowing the IR beam to reach the detector without interference from atmospheric gasses.

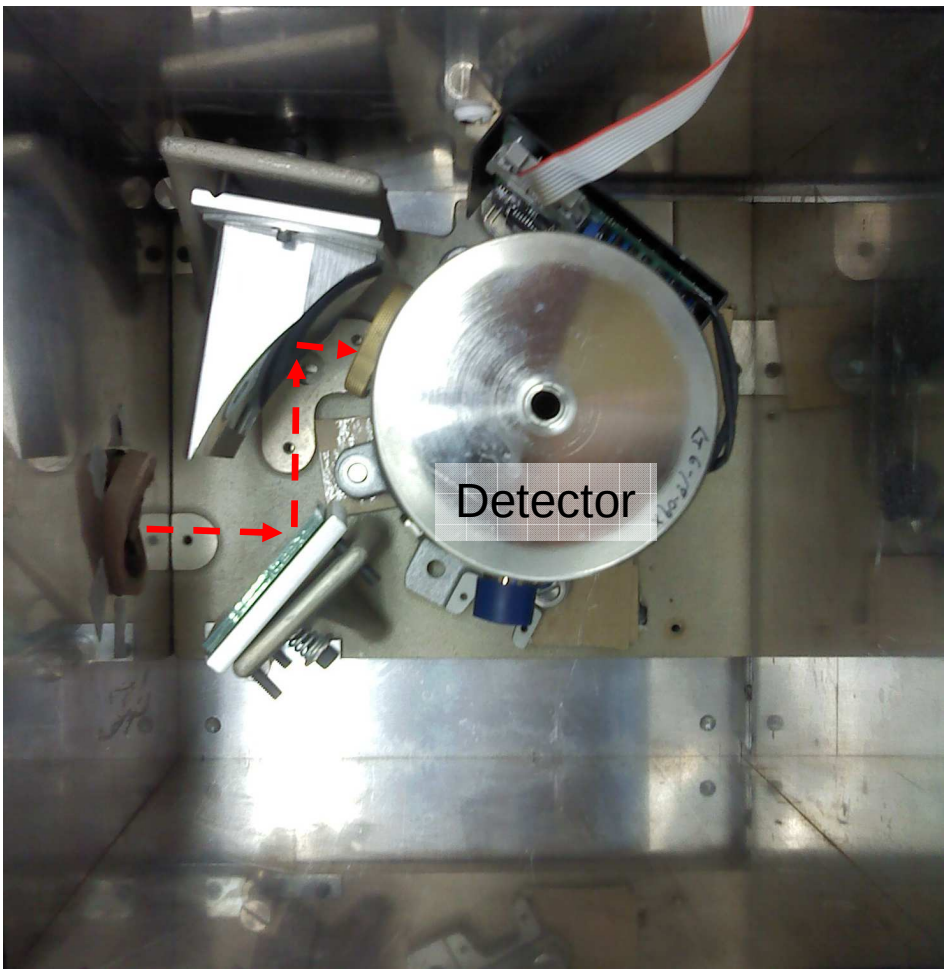

Figure 2.9: A top-down view of the detector box. The dashed line indicates the IR beam path.

Cylindrical potassium bromide (KBr) windows set in window flanges obtained from McAllister Technical Services, Inc. (www.mcallister.com, DPW275) allow the IR beam to proceed through the chamber while a vacuum is maintained inside the chamber. Fluorocarbon gaskets seal the KBr window to the flange and the Conflat flange on the window mount is connected to the chamber in the usual manner. A connection is built into the flange by the window seal allowing the flange to be differentially pumped. Polished 38mm x 6mm KBr discs were obtained from International Crystal Laboratories (www.internationalcrystal.net, 0002C-150). KBr is commonly used as a material for optics such as windows and beamsplitters due to

its transparency over a wide range of wavelengths from UV to IR. KBr is hygroscopic and should be protected from moisture. The interior of the chamber is typically maintained under vacuum and contains water at levels insufficient to affect the optical windows. However, atmospheric moisture could potentially damage the windows over time and, as such, the nitrogen-purged optics boxes are sealed against the IR window flanges to maintain the KBr in a dry environment. The windows and window mount allow the transmission of the IR beam through the instrument while providing a seal sufficient to maintain high vacuum conditions within the instrument.

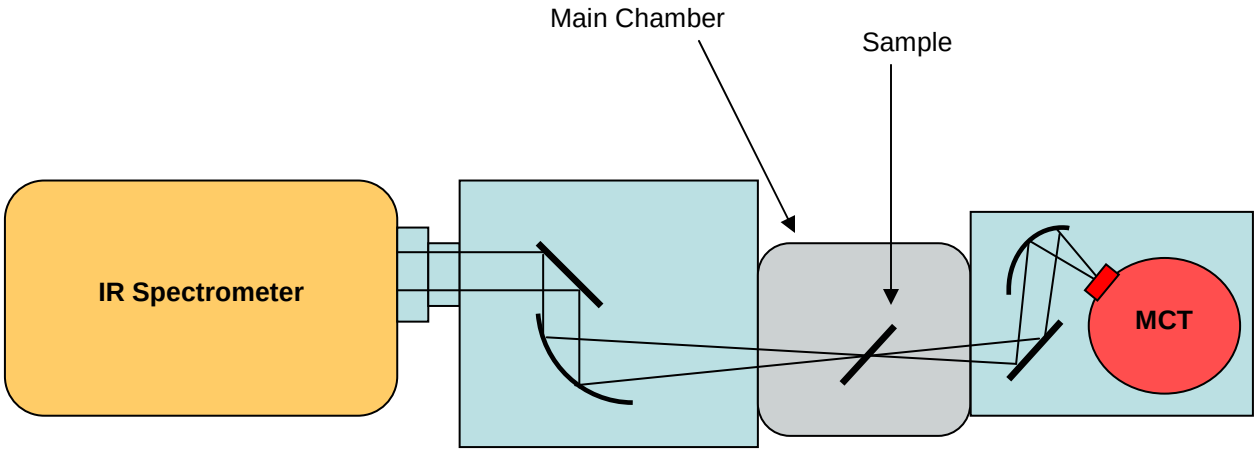

Figure 2.10: A ray-trace diagram of the complete IR path through the main chamber and both optics enclosures.

2.2.9 – Doser and Manifold

Since the bulk of experiments to be carried out on this system involve investigating gas-surface interactions, a method to dose the sample with a controlled amount of gas was needed. Due to the fast contamination time of the sample at atmosphere, the application of the gas on surface must be achieved while the surface is kept clean under vacuum. To provide the

capability to dose the surface with various gasses in a controlled manner under vacuum, a doser and manifold were designed and fabricated.

Doser – A custom doser (Figure 2.11) was constructed and attached to one of the 1.33" flanges of the main chamber. The doser was designed to apply a gas to the sample by providing a localized area of high pressure in close proximity to the sample. A 1.5" long section of 0.2" outer diameter stainless steel tube was pressed into the vacuum side of a 1.33" Conflat to ¼" VCR (vacuum coupling radiation) adapter. By making the end of the doser as close as possible to the sample, the gas leaving the doser impacts the sample at a greater concentration than the surrounding areas such as a different sample, the sample mount, or the chamber walls. This results in the sample surface experiencing a greater flux of dosed gas, thereby minimizing the time necessary to achieve a given concentration of adsorbed gasses on the sample. In addition, by directing the flow of gas at the surface, adequate dosing of the sample can be achieved with minimum contamination of ancillary surfaces, thereby keeping the pressure as low as possible during and after dosing. Although some of the dosed gas will impact other samples, the directional doser also helps to minimize this occurrence, keeping the other sample on the mesh as clean as possible for later experiments.

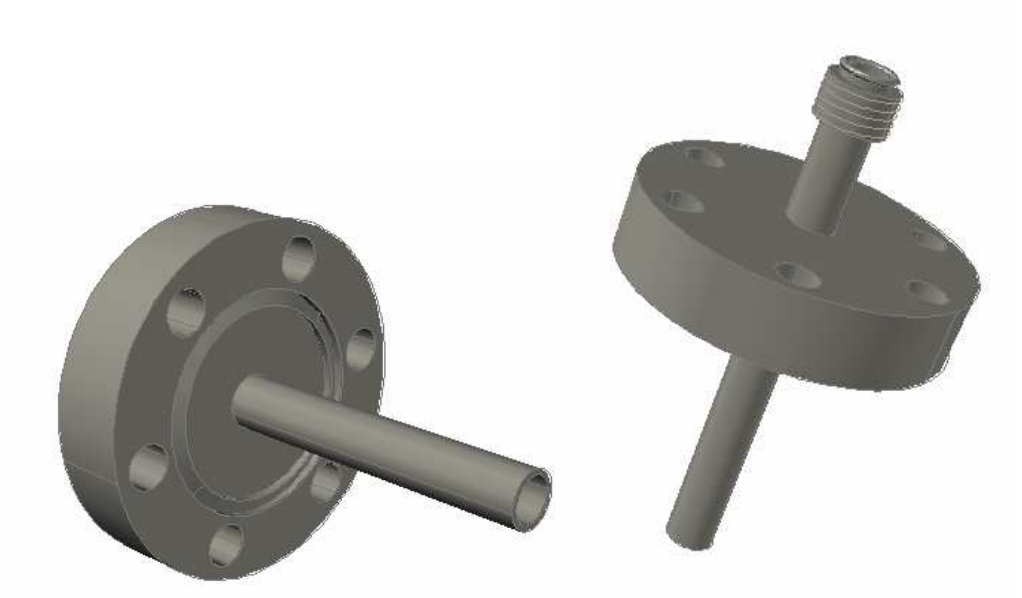

(a) **(b)**

Figure 2.11: Drawing of the doser. (a) Vacuum side of flange and knife edge visible (b) Atmosphere side of flange with VCR fitting.

The ¼" VCR coupling on the doser is connected to a valve that can be used to control the flux of gas that enters the doser. If experimental conditions require a lower flux of dosed gas or lower chamber pressure the flow of gas to the doser can be restricted by placing an aperture at the VCR connection between the valve and the doser. Various sizes of these apertures can be made by drilling a hole in a blank gasket used to make the VCR seal. While a drill press could be used for larger holes, laser drilled gaskets are available from Lenox Laser (www.lenoxlaser.com) ranging from 1-1000 micron aperture size for less than $100 each.

Manifold – The doser and control valve are connected to a manifold to facilitate the introduction of various gasses into the chamber. The doser and control valve are connected to a high vacuum region of the manifold which allows for vapor pressure dosing of CWA simulants. The high vacuum region is isolated from atmosphere using vacuum coupling radiation (VCR)

metal gasket face seal fittings which form a UHV-tight seal when a silver-plated stainless steel or nickel gasket is compressed between metal beads on the face of each fitting. While the portion of each VCR gland that makes the seal is genderless, the compression against the gasket is provided by the engagement of male and female nuts on either fitting. The main chamber and doser assembly can be used to evacuate that region of the manifold which helps to decrease the chance of interference caused by any molecules adsorbed to the interior surface of the manifold. To initiate the dosing process, the evacuated segment of the manifold is isolated from the chamber and the valve to a cylinder that contains a simulant is opened. After allowing the system to equilibrate, the simulant cylinder is isolated by closing the valve and the vaporous simulant in the manifold (concentration determined by the vapor pressure of the simulant) can be introduced into the main chamber for dosing. Opening the high pressure region of the manifold to the main chamber also provides the pumping necessary for freeze-pump-thaw cycles to purify the simulant or other liquid used for dosing. Future plans for expanding the capabilities of the manifold involve increasing from one to four isolable cylinders or glass bulbs which could contain other simulants or potential decontamination solutions. The expansion would also add a capacitance manometer that would make possible a precise determination of the pressure in the manifold, allowing for accurate quantitation of the dosed gas.

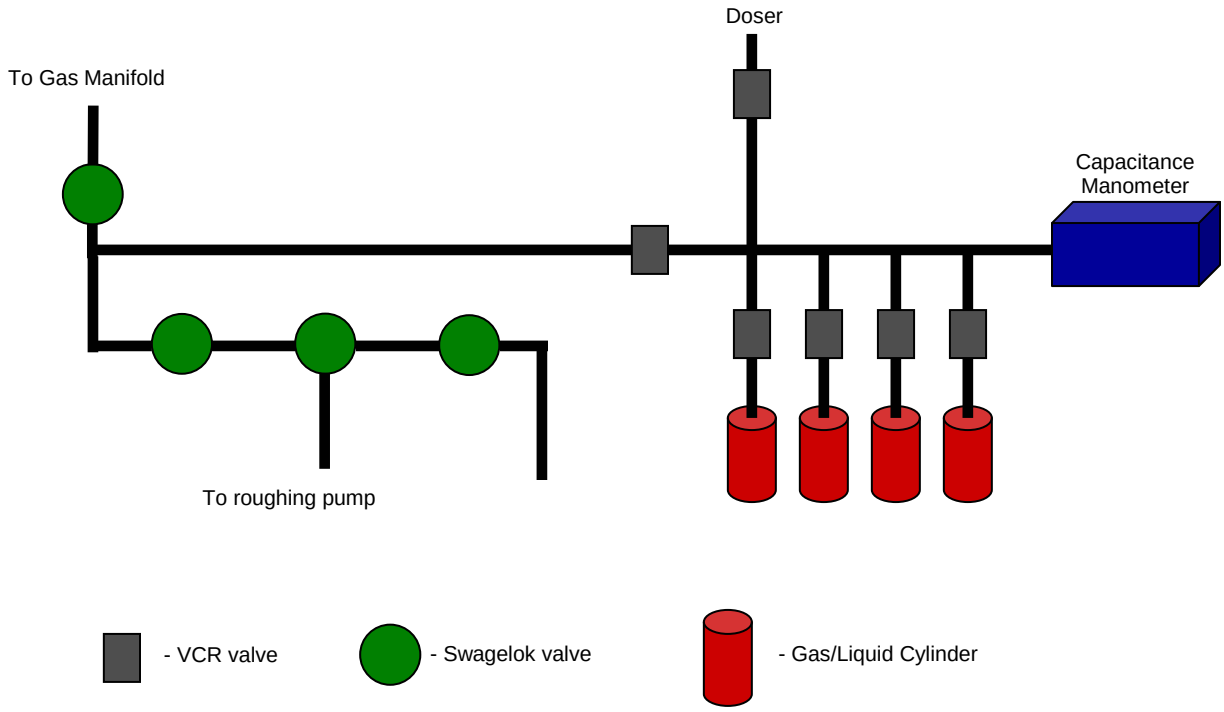

Figure 2.12: A diagram of the manifold. The CWA simulant is contained in the cylinders until needed for dosing. To dose the sample, the valve isolating the cylinder is opened to allow simulant vapor to fill the manifold. The valve to the doser is then opened, dosing the sample with simulant vapor.

A rough vacuum section of the manifold connected to the high vacuum portion of the manifold expands the connectivity and utility of the manifold. A Pfeiffer 15 l/min diaphragm pump serves as the roughing pump for the manifold, allowing evacuation of the manifold from atmosphere to rough vacuum in several seconds. In addition to providing rough pumping for the manifold, the rough vacuum region also connects to a previously constructed gas manifold in our laboratory, allowing the dosing of oxygen to clean the surface, as well as other gasses that could be used for a variety of experiments. Capabilities of the manifold can quickly and easily be expanded using the open ¼" Swagelok tube fitting. Both high and rough vacuum regions of the

manifold can be baked out with heat tape to encourage the removal of molecules adsorbed to the interior of the manifold, lowering the base pressure and reducing the possibility of contamination when dosing with different simulants or gasses. The manifold design provides a quick and convenient method to introduce various gasses to the doser, as well as providing standard connections to accommodate the expansion of the manifold for other types of experiments.

2.2.10 – Layout and Support

To position the chamber and ancillary equipment in an orientation conducive to operating the apparatus, it was necessary to develop a structure to support the chamber, pumps, and instrumentation. A steel frame cart serves as the main structure for the support system. Perhaps the most obvious role of this structure is to hold the chamber and pumps. To do this, a 1/4" thick aluminum plate was cut to fit within the frame of the cart and to increase the area of this support, slots were cut into opposite sides of the plate to allow the plate to extend outside of the cart. The plate is suspended within the frame of the cart by four pieces of 3/4" diameter threaded rod which are secured to the cart by nuts and extend downwards through the inside of the cart at each of the top corners. This design provides a simple and inexpensive solution to supporting the chamber and the threaded rod also provides the capability to translate the platform vertically. The ability to adjust the height of the chamber in relation to the IR spectrometer is crucial in aligning the beam path with the KBr windows and the sample. Since the internal compartment of the spectrometer was already in use for a separate research project on an adjacent table, it was decided to keep the spectrometer on the table and make the height of the chamber the adjustable factor. The platform provides sufficient support for the instrument and the adjustable height of the platform facilitates access to unused flanges in the event of the chamber being adapted for different types of experiments or expanded capabilities.

The platform provides a base to bear the weight of the chamber and the components connected to the chamber. The housing and control unit for both of the HiCube 80 pumping stations were placed on the platform and the diaphragm backing pump for each pumping station was relocated to the floor to avoid concerns regarding vibrations. The turbo/drag pumps for the main chamber and the RGA chamber are supported by the pumping station housing. The 4.5" Conflat flange on the turbo/drag pump was connected to a 4.5" to 2.75" conical reducer which is attached to the main chamber. A 4.5" to 2.75" zero-length reducer was used to connect the RGA chamber to the other turbo/drag pump. A lab jack resting on the housing for the second pumping station provided the support for this assembly. The RGA chamber, pressure gauge, and aperture were connected to the main chamber. This layout is illustrated in Figure 2.13. The IR windows and mounts were attached, along with the linear translation stage, sample mount, and feedthrough. A viewport on a 2.75" flange was connected to the unused 2.75" flange of the chamber to allow the operator to visually align the sample with the aperture and the IR beam path. The pressure gauge was connected to the front pumping station control unit that displays the pressure that the pressure gauge is reading, eliminating the need to purchase a separate reader. The resulting layout allows all the components to be connected in a compact design, providing the instrument with a minimal laboratory footprint. The compact design also provides a low internal volume facilitating a fast pumpdown time and low base pressure.

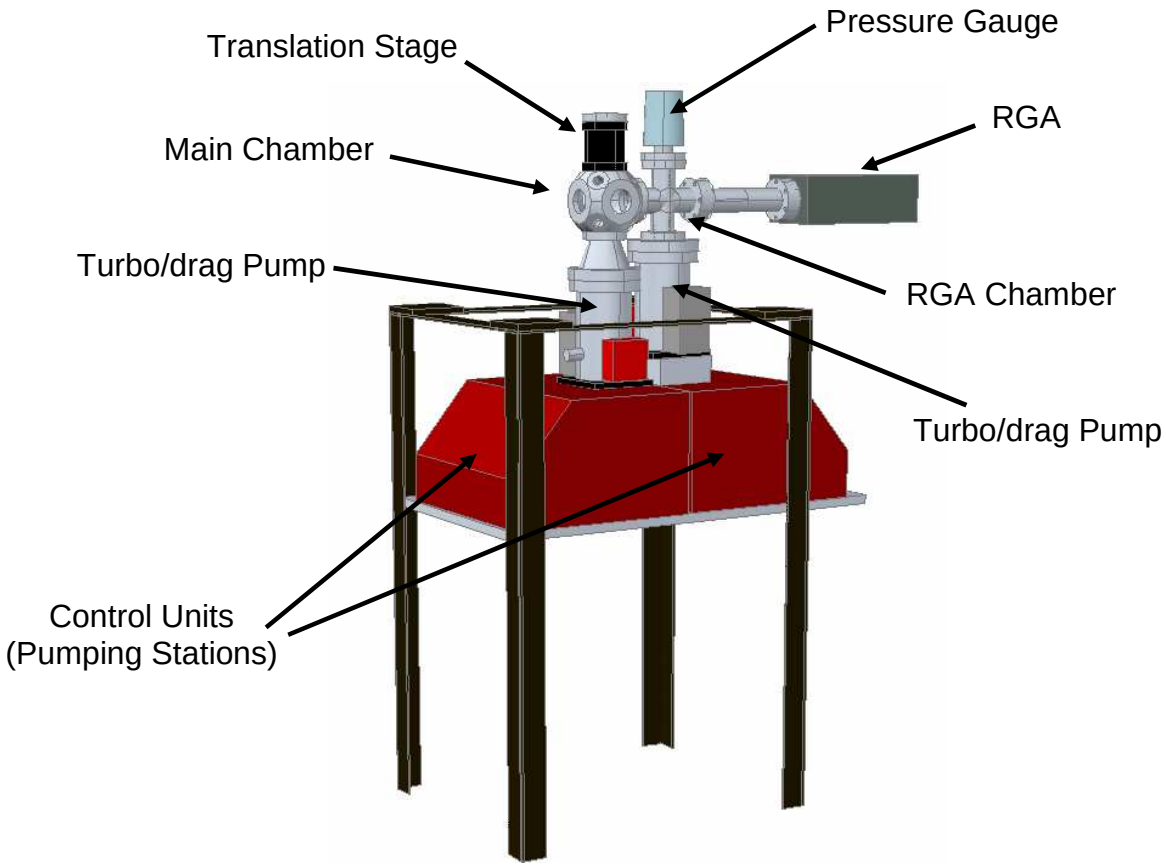

Figure 2.13: AutoCAD drawings of the system showing the arrangement of components of the instrument (Some components omitted).

In addition to providing support for the chamber, the cart was also used as a frame to mount the manifold and platforms for the optics enclosures. A piece of 1/8" sheet metal was cut to the appropriate dimensions and bolted to the right side of the cart. The manifold was then connected to the metal sheet and was positioned within reaching distance of the computer used to control the IR and RGA, affording the operator the ability to control the manifold while operating the analytical equipment. Aluminum plate was used to fashion platforms for the optics

enclosures. The platforms were attached with countersunk screws to the left and right top cross pieces of the cart providing a stable surface to support the optics enclosures.

2.3 - Summary

The design and construction of a new high vacuum instrument capable of studying metal oxide nanoparticles with a moderate sample throughput was accomplished and discussed. Infrared spectroscopy and mass spectrometry are the primary analytical methods used with this instrument. A custom-designed sample mount provides the support for nanoparticulate samples as well as rotational and vertical manipulation of the sample. The sample mount also provides the ability to cool and heat the sample over a range from 125 – 700 K. The controlled application of chemical warfare agent simulants or other relevant gases is achieved via a directional doser and manifold. These components function to provide an instrument capable of studying interactions between gasses and nanoparticulate surfaces.

Table 2.2: Instrument Specifications.

Pumps and Pumping Speed	
Turbomolecular (2)	67 l/s
Diaphragm (3)	0.25 l/s
Base Pressure	~10^{-9} torr
Operating Pressure	10^{-4} – 10^{-9} torr
Pumpdown Time – 760 to 10^{-7} torr	~ 30 minutes
Infrared Spectrometer	Nicolet Nexus 470 E.S.P
Resolution	15.4 cm^{-1} – 0.24 cm^{-1}
Detector	Liquid nitrogen cooled, MCT-A
Sample Temperature Range	~150 K – 800 K
Estimated Sample Throughput for TPD Experiment	5-10/day

Overall, the instrument is capable of providing data from a variety of experiments aimed at the fundamental understanding of the interactions of chemical warfare agent simulants and nanoparticulate surfaces. However, the primary objective of the design and construction of this high vacuum instrument was not just to provide an instrument with the ability to perform fundamental gas-surface studies, but to exploit various design aspects to increase the rapidity and ease of those studies, especially with regards to sample loading and pumpdown times. In addition to the increased sample throughput and relative ease of operation, the chief advantages of this instrument over ultrahigh vacuum systems of comparable capability is that the instrument discussed in this work is an order of magnitude less expensive (~ $70,000) and has a

significantly smaller laboratory footprint. The smaller size of the chamber and small footprint are of significant interest if actual chemical warfare agent studies are concerned. The chamber is small enough to fit inside a standard fume hood with some minor modifications to the placement of pumps, support structure, and IR spectrometer. By placing the entire system within a fume hood, many safety-related design and engineering considerations are eliminated, providing a comparatively safe, simple, fast, and inexpensive way to carry out fundamental high vacuum studies of chemical warfare agents and surfaces. Although studies involving CWAs or other toxic chemicals may not be in the future plans for work at Virginia Tech, the instrument provides our research group with a new, higher-throughput tool to investigate gas-surface interactions.

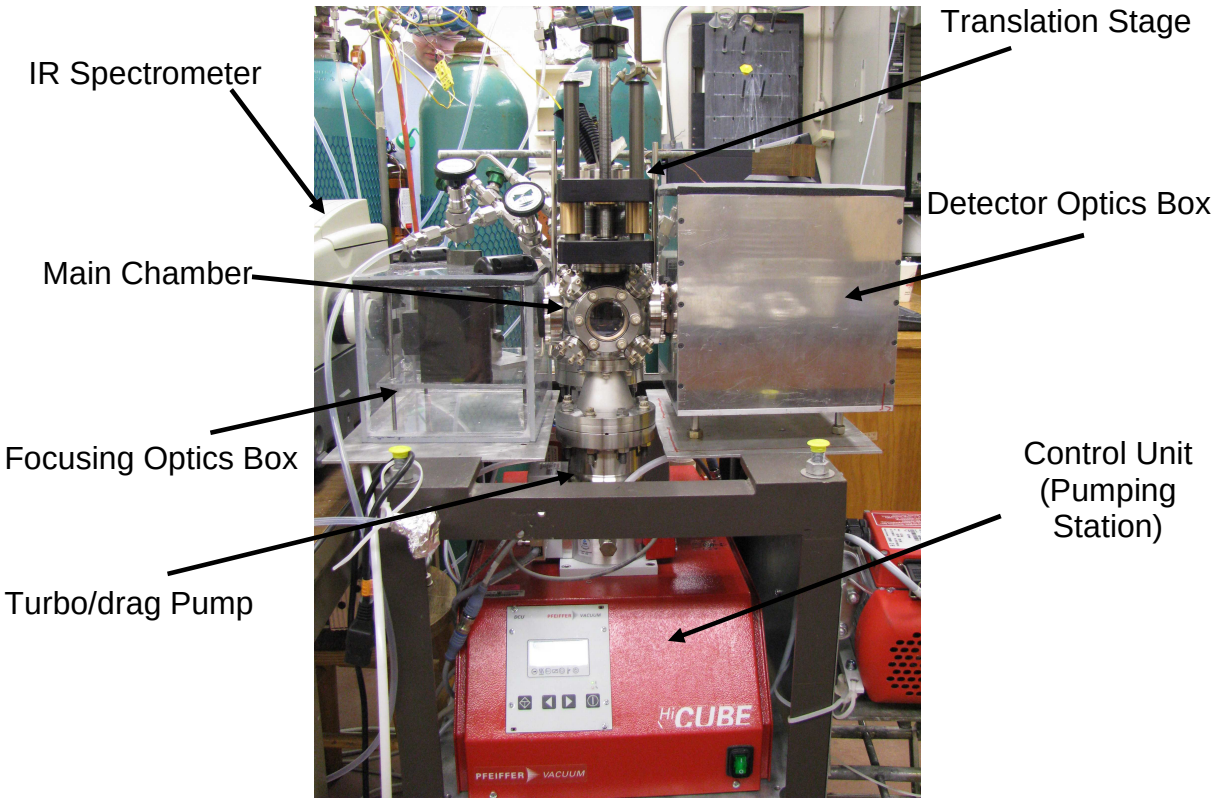

Figure 2.14: A picture of the system showing the optics enclosures, main chamber, translation stage, main chamber turbo/drag pump, and the pumping control unit, as seen from the front.

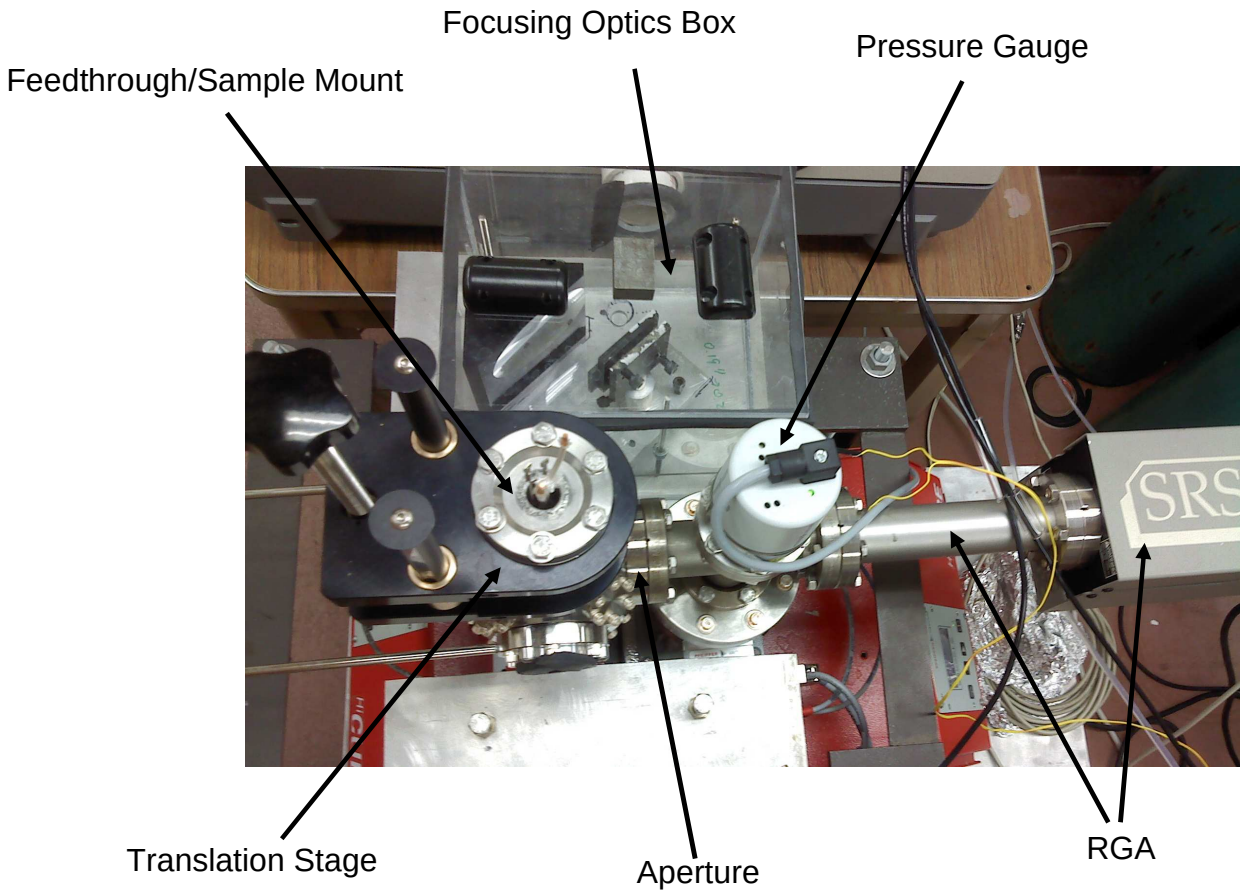

Figure 2.15: A top-down view of the system. The detector optics enclosure is not present in this image.

Chapter 3 – Adsorption of DMMP to Silica Nanoparticles: Temperature Programmed Desorption using Infrared and Mass Spectrometry

Initial experiments were conducted to assess the performance of the instrument by comparing the results achieved in the present study to results available in the literature. The instrument was designed to study interactions of chemical warfare agent (CWA) simulants with nanoparticulate surfaces; therefore, initial experiments were carried out using the CWA simulant dimethyl methylphosphonate (DMMP) and a nanoparticulate silicon dioxide surface. The wide use of DMMP as a CWA simulant made it a prudent choice and silica nanoparticles were chosen as the substrate due to the availability of both experimental and theoretical data for the DMMP-SiO_2 system. Previous studies have demonstrated the ability of nanoparticulate metal oxides to decompose CWA simulants; however, the limited reactivity of silicon dioxide towards organophosphonates like DMMP was exploited to avoid any convolution of initial results through decomposition of the simulant.

3.1 Introduction

Many metal oxide nanoparticles have been shown to adsorb and decompose chemical warfare agents and their simulants. Unlike metal oxides such as TiO_2,[25, 30, 59] La_2O_3,[23] MgO,[23, 59] Al_2O_3,[59] WO_3,[59, 60] and CaO,[15] SiO_2 is unique in that molecular desorption of DMMP is observed at elevated temperatures.[22] The limited reactivity of nanoparticulate silica makes it an excellent material to non-destructively sorb chemical warfare agents and simulants, facilitating studies to determine interactions such as binding energy and orientation. Silica has also been investigated by Tripp et al.[61] as a potential sorbent for a selective CWA detector and by Panayotov et al.[62] as

a component of a destructive sorbent for the mustard gas simulant 2-chloroethyl ethyl sulfide (2-CEES).

Benchmark tests were performed to evaluate the performance of the newly constructed instrument by comparing initial results to existing data. DMMP and silicon dioxide were chosen for initial studies due to the significant body of data that exists for the DMMP-silicon dioxide system. All infrared modes are known and the activation energy of desorption has been calculated through experimental and theoretical studies. Tripp[61] used infrared spectroscopy in an attempt to reveal the binding configuration of DMMP on a thin film of nanoparticulate silica and concluded that adsorption occurs via hydrogen bonding between surface silanol groups and the methoxy groups of DMMP. Henderson et al.[22] used Auger electron spectroscopy (AES) to study DMMP-SiO_2 interactions and experimentally estimated the activation energy of desorption for DMMP on silica for monolayer and multilayer states using temperature programmed desorption (TPD). Computational work by Bermudez has provided a theoretical estimate of the activation energy of desorption, as well as infrared absorption frequencies and assignments, for various binding configurations of DMMP on silicon dioxide.[63]

Tripp's approach towards understanding the binding properties of DMMP to silica involved studying the IR spectra during the adsorption and desorption of the simulants DMMP, trimethyl phosphate (TMP), methyl dichlorophosphate (MDCP), and trichlorophosphate (TCP). These CWA simulants, depicted in Figure 3.1, each have a different number of methoxy groups attached to the central phosphorus atom. By comparing the gas-phase spectra of these simulants to that of the adspecies, as well as comparing the differences of these spectra for each simulant, Tripp was able to use IR spectroscopy to draw conclusions as to the binding configuration of

DMMP on silica. Tripp suggested that adsorption occurs via hydrogen bonding between the methoxy oxygen of DMMP and surface bound –OH groups.

The shift in frequency of IR absorbing modes from the gas phase to the adsorbed phase can also provide valuable information about a species adsorbed to a surface. Upon adsorbing to silica, the DMMP ν(P=O) mode redshifts 19 cm^{-1} from the gas phase[61], as opposed to a shift of 52-200 cm^{-1} for WO_3, TiO_2, Al_2O_3, MgO, La_2O_3, and Fe_2O_3.[23, 59, 64] Tripp suggests this shift may be due to electronic effects. However, given that silica does not decompose DMMP like other metal oxides, it would not be unexpected to observe a weaker bonding interaction even if adsorption occurs via the same functional group. In addition to observing shifts in the vibrational frequencies of an adsorbed molecule, shifts in vibrational modes of the surface also occur upon adsorption of a molecule. A shift in the SiO-H stretch to lower energy is observed when non-hydrogen bonded silanol groups become hydrogen bonded to an adsorbed species; the greater the ν(O-H) shift, the stronger the hydrogen bond. For difference spectra, this shift results in a sharp negative peak around 3747 cm^{-1} as the "free," non-hydrogen bonded –OH groups are replaced by hydrogen bonded groups with a broad peak typically centered in the 3700-3100 cm^{-1} region. Tripp also notes that, upon evacuation, the desorption temperature for TCP, MDCP, DMMP, and TMP increases with the number of methoxy groups in each simulant, suggesting a correlation between hydrogen bonding strength and desorption temperature. By constructing an instrument that can use IR and MS simultaneously, we hope to learn how such vibrational frequency shifts (measured by IR) are correlated with the desorption energy (measured by TPD).

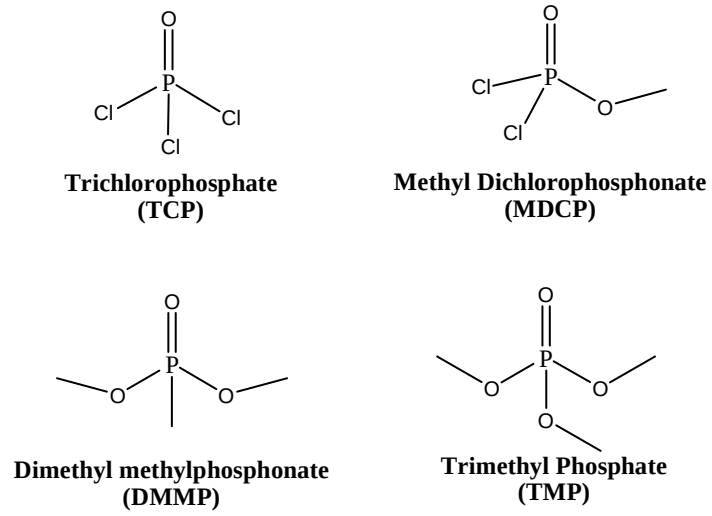

Figure 3.1: The structures of various CWA simulants.

Computational work done by Bermudez[63] suggests that DMMP, Sarin, and trichlorophosphate hydrogen bond to –OH groups on silica, not through the methoxy as proposed by Tripp et al.,[61] but via the oxygen atom of the P=O group, the same way DMMP adsorbs on other metal oxides. The most stable adsorption pathway for all three gases was found to be through two silanol groups and the bidentate P=O group, as shown in Figure 3.2 (b). Bermudez' calculations suggest a metastable state might exist with hydrogen bonding to both the P=O and the $–OCH_3$, however the bonding to either functional group interferes with the bonding to the other. This binding configuration has a calculated ΔE_{ads} value of −10.1 kcal/mol whereas hydrogen bonding to the methoxys and P=O have calculated ΔE_{ads} values of −15.1 and −21.6 kcal/mol, respectively.[63] A comparison of the experimentally determined $\Delta\nu$(P=O) value[61] of −19 cm^{-1} to the computed values[63] for phosphoryl- and methoxy-bound configurations of -29 cm^{-1} and +7 cm^{-1}, respectively, supports the argument for phosphoryl binding to the silanol groups.

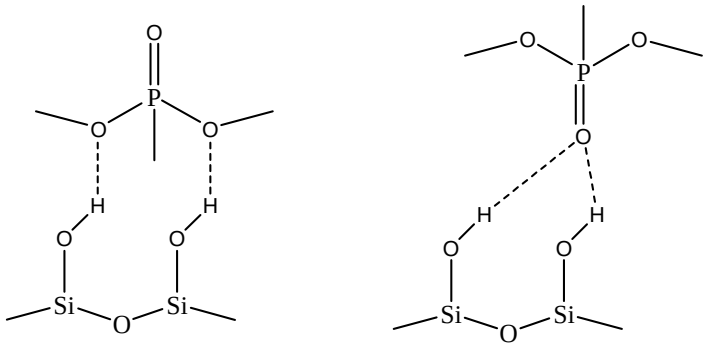

(a) **(b)**

Figure 3.2: Possible adsorption geometries for DMMP on silica. Surface hydroxyls hydrogen bond to DMMP through either (a) the methoxys or (b) the phosphoryl oxygen.

It is apparent that further experimental work is needed to elucidate the binding configuration of DMMP on silica. The present work is, to the author's knowledge, the first TPD study of DMMP on silica using a combination of infrared and mass spectrometric methods. While data is normally obtained during a TPD experiment using a mass spectrometer to detect and identify desorbing species, infrared spectrometry can also be applied in the same experiment to monitor the changes in surface-bound species. By following the changes in the infrared spectra, we are able to monitor specific chemical bonds throughout the experiment. This powerful technique is applied to DMMP on silica with the aim to answer questions in the literature about the binding interactions in this system.

3.2 Experimental

3.2.1 Instrument Design Overview

An instrument with infrared spectroscopic and mass spectrometric capabilities was developed to study interactions between CWA simulants and nanoparticulate surfaces under high vacuum (10^{-6} – 10^{-9} Torr). Nanoparticles were pressed onto a tungsten grid to form a sample spot. The tungsten grid was positioned in the main chamber by attachment to copper leads from a vacuum feedthrough. Thermal manipulation of the sample was achieved by Ohmic heating or conductive cooling. The application of CWA simulants to the nanoparticulate surface was achieved using a directional doser. Infrared spectroscopy and mass spectrometry was conducted to monitor adsorption and desorption processes on the sample surface.

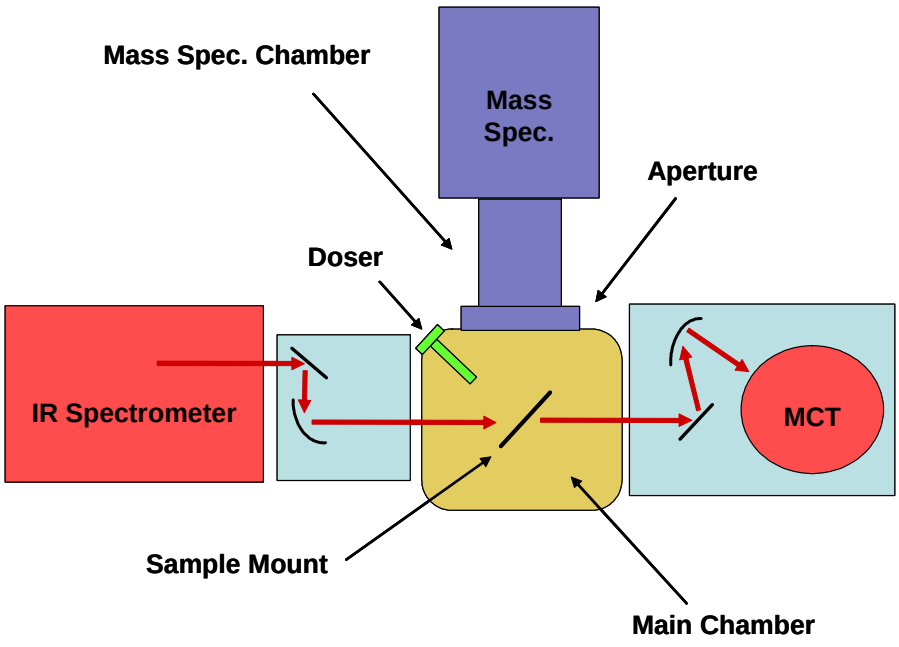

Figure 3.3: A top-down view depicting the basic arrangement of the instrument.

3.2.2 Chemicals and Reagents

Aerosil® 200 silica nanoparticles (surface area: 200 m^2/g; particle diameter: 12 nm) were purchased from Spectrum Chemicals and Laboratory Products and were used without further preparation outside of the vacuum chamber. Dimethyl methylphosphonate (DMMP, ≥ 97% pure) was purchased from Fluka. HPLC grade methanol and acetone were purchased from Fisher Scientific and used as received. Deionized water (18.2 MΩ) was prepared using a Millipore purification system. The tungsten mesh used as the sample support was obtained from Buckbee-Mears Co.

3.2.3 Preparation

Mesh and sample - A portion of tungsten mesh was cut to fit the sample mount and then cleaned by ultrasonic agitation in methanol followed by ultrasonic agitation in acetone. The mold and piston for pressing the nanoparticles into the mesh were also cleaned in the same manner. The tungsten mesh was then secured to the mold and ~5mg of the silica nanoparticles were added to the mold. The piston was placed in the mold, on top of the nanoparticles and the assembly was compressed at 13,000 psi for 2 minutes using a hydraulic press. The mesh was then removed from the mold and, upon visually verifying the nanoparticles were securely pressed onto the mesh, the mesh was affixed to the copper sample mounts as described previously (Section 2.2.6). Bare chromel and alumel wires (0.005 inch diameter, 36 AWG) were spot welded to the appropriate lead on the feedthrough and then welded to form a junction. The junction was then spot welded to the mesh above the silica nanoparticles. The sample mount was positioned in the chamber in the appropriate orientation and the chamber was evacuated. A variable autotransformer was connected to the power leads on the atmospheric side of the

feedthrough and a thermocouple controller was attached to the thermocouple leads using insulated 0.020 inch diameter (24 AWG) chromel and alumel wire.

SiO_2 Cleaning – Contaminants on the surface of the silica nanoparticles were removed by heating the sample to 450 °C under high vacuum ($\leq 10^{-6}$ torr) for 30 minutes. This procedure not only removes adsorbed water and organic molecules but also reduces the amount of hydrogen-bonded hydroxyl groups, yielding the active, isolated hydroxyl groups on the surface.[60, 61, 65] Elimination of water from hydrogen-bonded Si-OH groups provides the active sites for DMMP adsorption.[66]

DMMP – Approximately 15 ml of DMMP was transferred to a glass bulb which was then attached to a bellows-sealed valve attached to the gas doser. The DMMP was purified using three freeze-pump-thaw cycles, pumping for 30 minutes while the bulb was submerged in liquid nitrogen. The valve was closed to isolate the bulb from the chamber and the DMMP was allowed to warm to room temperature.

3.2.4 Data Collection

Transmission IR - Transmission infrared spectroscopy was performed using a Nicolet Nexus 470 FT-IR spectrometer configured for use with an external, liquid nitrogen cooled MCT-A detector. As described in section 2.2.8, optical mirrors in a nitrogen-purged enclosure direct the beam through a KBr window into the chamber and focus the beam on the sample. The beam exits the chamber through a KBr window and is focused on the detector by another pair of optical mirrors in a nitrogen-purged enclosure. Each spectrum recorded under steady state conditions consists of an average of 128 scans while spectra recorded during heating ramps consist of 20 scans. All IR spectra are recorded with a resolution of 2 cm^{-1}. Difference spectra were collected by subtracting a background spectrum of the silica and tungsten mesh from a

spectrum of the same surface after altering the conditions (e.g. dosing with DMMP or heating to cause desorption).

Mass Spectrometry - Mass spectra were recorded using a Stanford Research Systems Residual Gas Analyzer 300 with an electron multiplier. The filament current at the electron ionizer was 1 milliamp and the electron energy was 70 eV with a focus voltage of 90 volts. The channel electron multiplier was operated at 1781 volts with a gain of 8130. A 4 mm aperture between the main and mass spectrometry chambers decreases background signal in the mass spectra by deflecting errant molecules. During dosing experiments, differential pumping maintained the mass spectrometry chamber at a lower pressure than the main chamber. This allowed for the operation of the residual gas analyzer even when the pressure in the main chamber was outside of the operable range.

3.2.5 Temperature Programmed Desorption

Vapor pressure dosing of silica with DMMP for the TPD experiment was achieved by opening a valve separating the doser and glass bulb containing DMMP. The vaporous DMMP entered the chamber through the doser. During dosing, the pressure in the RGA cross was maintained at 5.6×10^{-6} torr and the silica sample was maintained at room temperature. Difference spectra were recorded with the IR spectrometer and dosing was continued until no further change in the spectrum was observed. The valve was then closed and the pressure was allowed to decrease to 6.5×10^{-8} torr before the heating ramp was initiated. The heating ramp was carried out using a power supply and proportional-integral-derivative (PID) controller. Sample temperature monitoring and feedback for the PID was provided by a type K thermocouple spot-welded to the tungsten mesh.

3.3 Results and Discussion

3.3.1 Adsorption of DMMP on Silica

Infrared Spectroscopy – The infrared spectrum of silica before dosing with DMMP is shown in spectrum (A) of Figure 3.4. The strong absorbance of silica below 1200 cm^{-1} due to IR-active phonons occludes IR active modes of DMMP in that region, such as the phosphoryl stretching mode. Combination bands of the silica vibrations are located around 2000-1600 cm^{-1}. The absorption spectrum of silica remains largely unchanged after dosing and subsequent thermal desorption of DMMP in a TPD experiment.

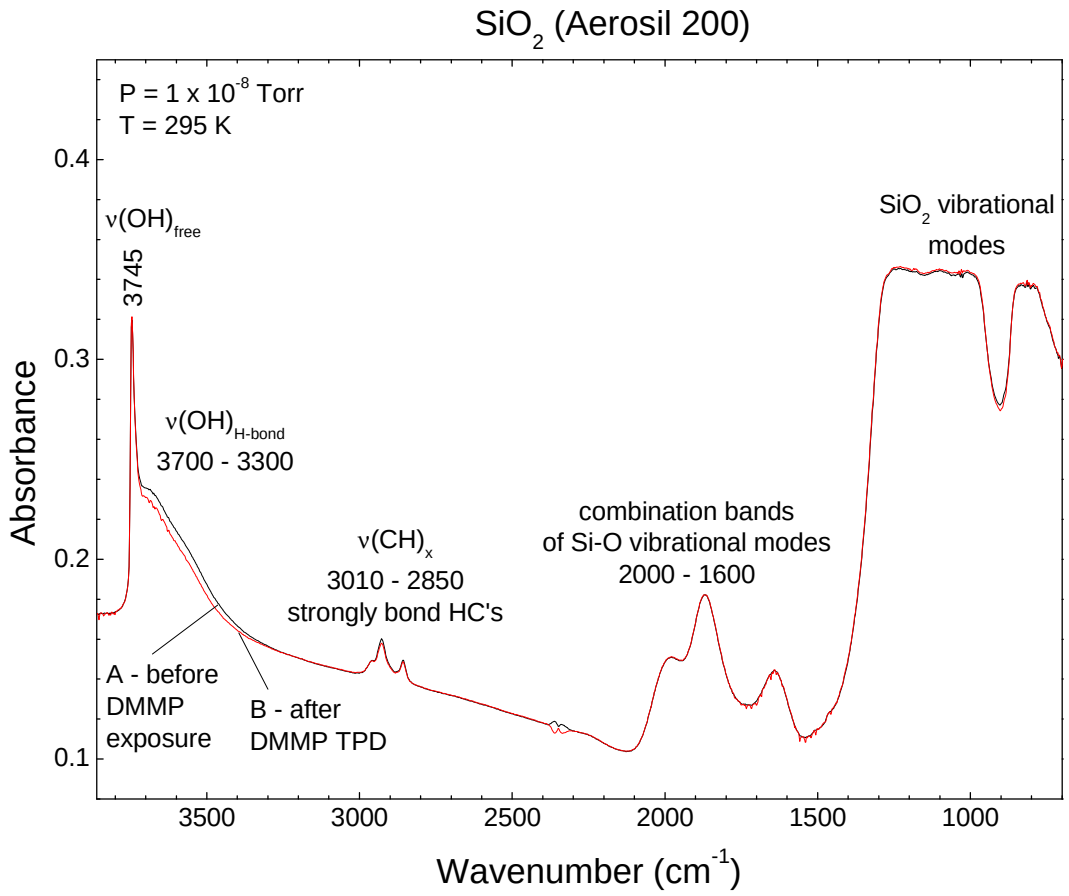

Figure 3.4: Infrared spectrum of silica before DMMP exposure (A) and after temperature programmed desorption of DMMP (B), showing a minimal change in absorbance after thermal desorption of the adsorbed species.

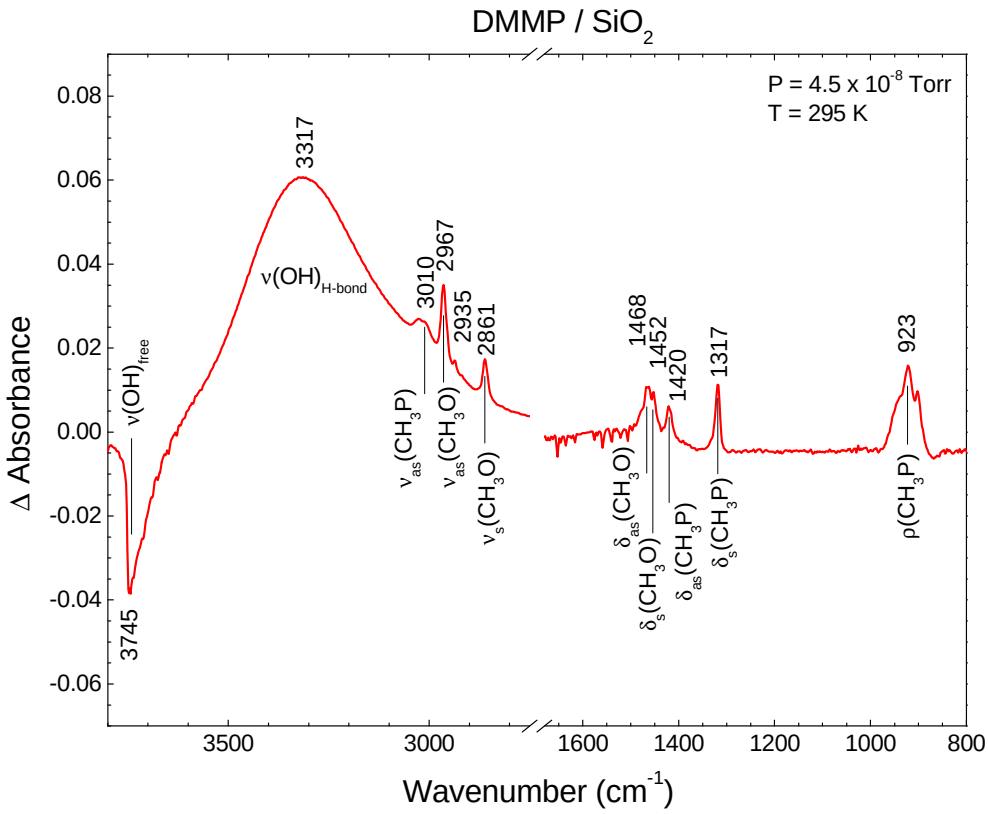

Figure 3.5: Difference infrared spectrum of vaporous DMMP deposited on nanoparticulate silica. The spectrum of clean silica (prior to dosing) was subtracted from the spectrum of DMMP adsorbed on silica (after dosing) to yield the above figure. Non-zero ΔAbsorbance values indicate the appearance (positive ΔAbsorbance) or disappearance (negative ΔAbsorbance) of IR-active modes. No significant changes were observed from 2900 cm^{-1} to 1650 cm^{-1} and data in that region was omitted.

The difference spectrum after dosing the silica with DMMP is shown in figure 3.5. Changes in the absorbance in the ν(C-H) region (3000-2800 cm^{-1}) are consistent with DMMP adsorbed on silica. The sharp negative band at 3745 cm^{-1} shows the decrease in non-hydrogen bonded, "free" –OH groups on the surface of the silica and the broad ν(O-H) peak centered at

3317 cm^{-1} results from the hydrogen bonding of the surface hydroxyls with DMMP. The observed ν(O-H) shift of −428 cm^{-1} is consistent with the computed values for hydrogen bonding via the methoxy (−423 cm^{-1}) or phosphoryl (−420 cm^{-1}) groups,[63] but is not in close agreement with the previous experimentally obtained value of −524 cm^{-1}.[61] Larger ν(O-H) shifts have also been observed in other research within our group while studying the same system and it seems the magnitude of this shift is affected by the surface coverage of both the free hydroxyl groups and DMMP.

Mass Spectrometry – Mass spectrometry was used to detect and identify gas-phase molecules from dosing or desorption experiments. The mass spectrum collected during dosing detected ions at m/z ratios of 109, 94, 79, 63, and 47 that are characteristic of the DMMP fragmentation pattern.[67] The mass spectrometer provided the ability to monitor the partial pressure and identity of molecules that desorbed from the sample during TPD experiments.

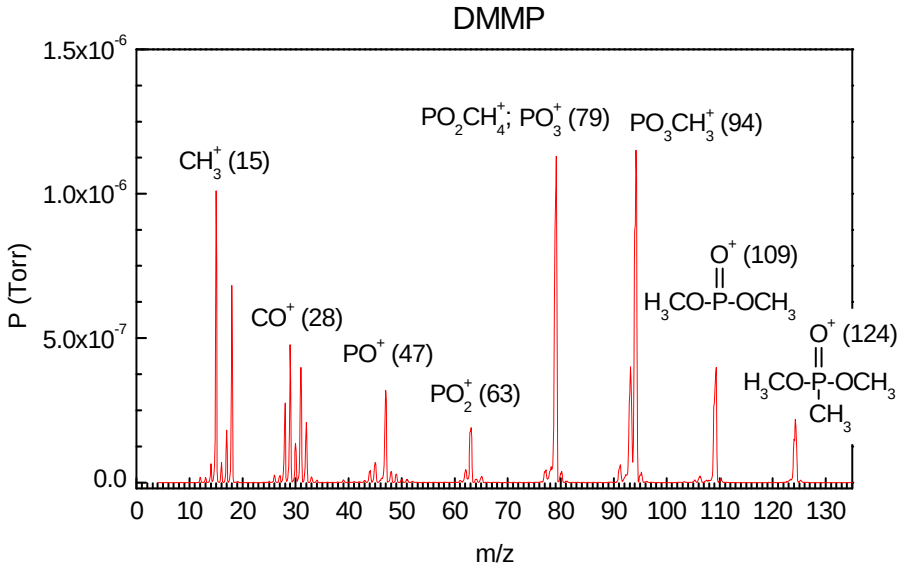

Figure 3.6: Mass Spectrum collected while dosing silica with DMMP. Assignments of molecular fragments were made with assistance of reference 67.

3.3.2 Temperature Programmed Desorption

To determine the adsorption energy for DMMP on silica, a TPD experiment was performed. The surface was heated at a rate of 0.4 K/s from 300 to 675 K. During this time, the mass spectrometer was used to record the signal for DMMP fragments of m/z = 94, 79, 63, and 47. The TPD trace for each mass is displayed in figure 3.7 and reveals a peak desorption temperature, T_p, of 375 K.

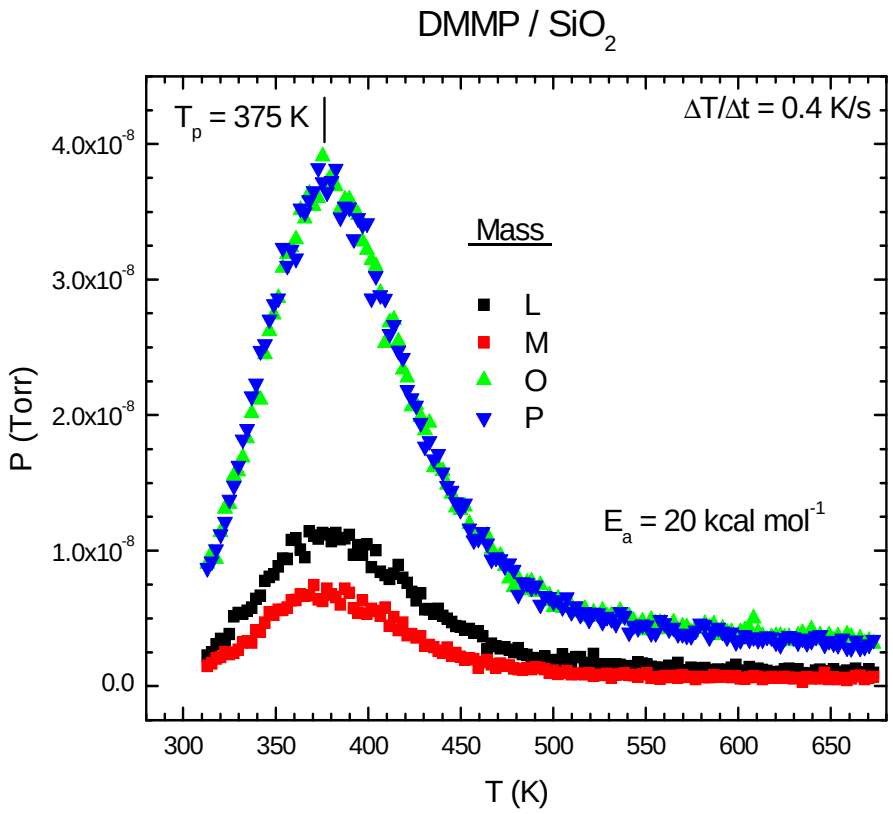

Figure 3.7: The TPD trace of DMMP on SiO_2. Mass spectrometry data was recorded for fragments of DMMP at m/z ratios at 47 (PO^+), 63 (PO_2^+), 79 ($PO_2CH_4^+$; PO_3^+) and 94 amu ($PO_3CH_3^+$).

In 1963, Redhead[68] showed that the results of a TPD experiment could be used to calculate the activation energy for desorption, E_a, using equation 3.1,

$$-\frac{E_a}{k_b T_p} = \ln\left(\frac{\beta}{k_b T_p^2}\right) + \ln\left(\frac{E_a}{\upsilon \theta_p^{n-1} n}\right) \tag{3.1}$$

where k_b is the Boltzmann constant, β is the heating rate in K/s, θ_p is the surface coverage at T_p, n is the order of the reaction, and υ is the pre-exponential factor. Du et al. noted that, within reasonable approximation, equation 3.1 can be rearranged to form equation 3.2, where θ_0 is the surface coverage at the start of the temperature ramp.[69]

$$-\frac{E_a}{k_b T_p} = \ln\left(\frac{\beta}{k_b T_p^2}\right) + \ln\left(\frac{E_a}{\upsilon \theta_0}\right) \tag{3.2}$$

By repeating the TPD experiment using different temperature ramp rates, an Arrhenius plot can be constructed by plotting $1/T_p$ against $\ln(\beta / T_p)$. The slope of this line is approximately equal to the activation energy.[70] Although this approach requires the TPD experiment to be performed using multiple heating rates, Equation 3.3 can provide a reasonable approximation of the desorption energy with data from a single heating rate.[68]

$$E_a / RT_p = \ln\frac{\upsilon T_p}{\beta} - 3.64 \tag{3.3}$$

The attempt frequency, also referred to as the pre-exponential factor, must be assumed or calculated via other methods. Wilmsmeyer et al.[71] have experimentally measured the attempt frequency for the same DMMP-SiO_2 system to be approximately 1.5×10^{10} s^{-1}. Using Equation 3.3, I calculated the E_a to be 20 kcal/mol, based on the TPD data of Figure 3.7.

In addition to conducting TPD studies by detecting desorbed species with a mass spectrometer, IR spectra can be used as the analytical method for TPD studies. In an IR TPD experiment, the sample is heated at a constant rate, as in a conventional TPD experiment. As a

species desorbs from the surface of the sample, a decrease in absorbance is observed. The region where the decrease occurs corresponds to the IR active regions of the adsorbed species. By calculating the rate of change in IR absorbance in certain regions, we can determine the rate of desorption of specific species, apply a Redhead-type analysis, and determine the desorption energy of that species. IR spectroscopy enables one to identify which bonds break during desorption processes. This may facilitate the identification of the desorbed species but also allows for the determination of the desorption energy for a specific binding site or binding configuration, leading to a better understanding of the desorption mechanism.

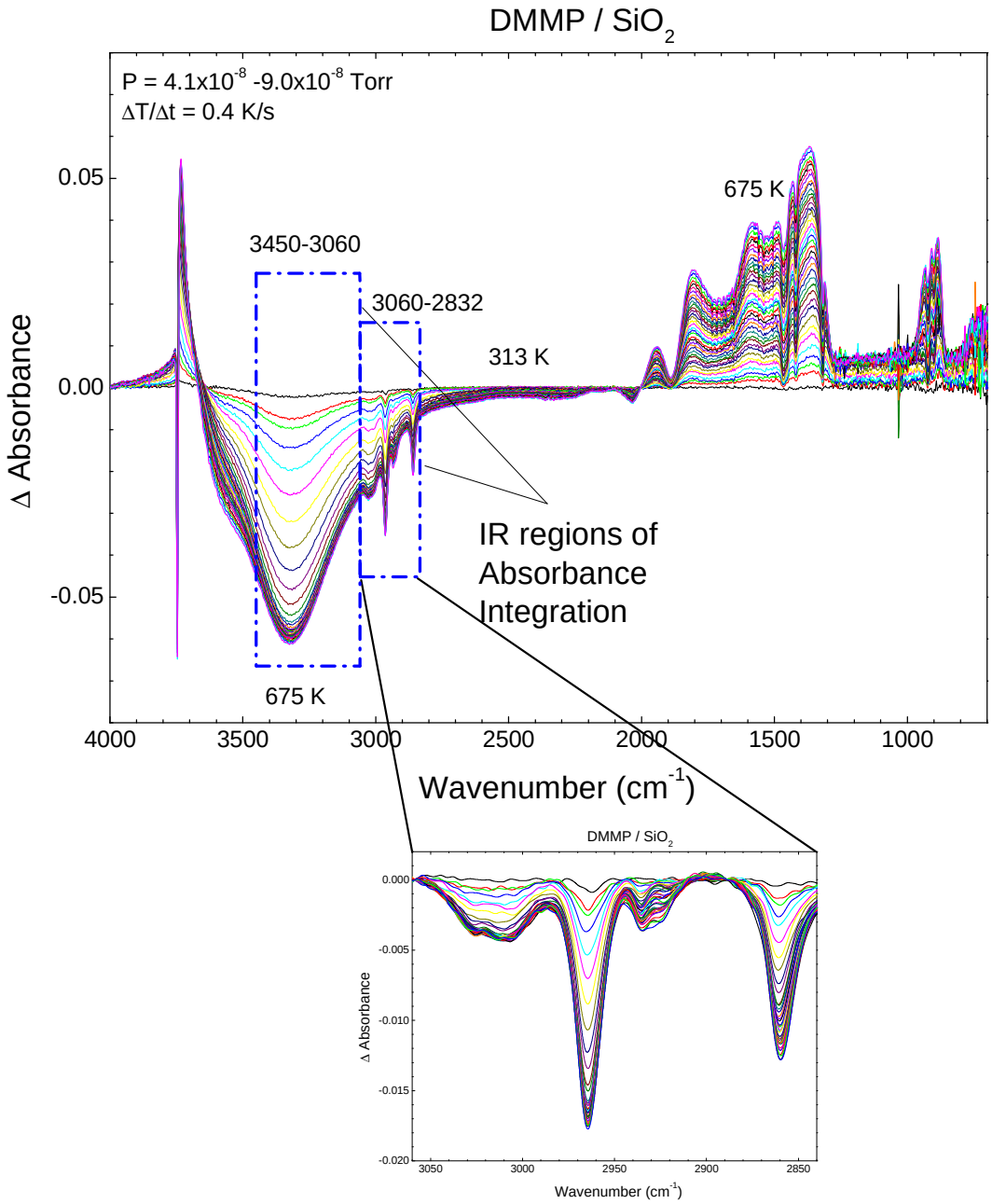

Figure 3.8: Difference spectra of DMMP desorbing from SiO_2 during a heating ramp from 313 K to 675 K. The $\nu(O\text{-}H)_{H\text{-}bond}$ (3450-3060 cm^{-1}) and $\nu(C\text{-}H)$ (3060-2832 cm^{-1}) DMMP modes decrease in absorbance as temperature increases. The sharp negative peak at 3747 cm^{-1} is attributed to a redshift in the $\nu(O\text{-}H)_{free}$ modes due to thermal effects.

Difference spectra (Figure 3.8) were used to construct a TPD trace with IR data. The IR absorbing region for the hydrogen bonded ν(O-H) mode at 3450-3060 cm^{-1} and the ν(C-H) region at 3060-2832 cm^{-1} were used to quantify the change in DMMP coverage. The change in integrated area for each difference spectrum (Δ[Integrated ΔA]) was recorded for each of these regions and plotted with respect to temperature (Figure 3.9). An increase in absorbance of Si-O lattice modes (below 2000 cm^{-1}) was attributed to optical effects during sample heating and is reproducible without DMMP adsorbed to the sample. These bands exhibit a linear change in integrated area with respect to temperature as would be expected for a linear temperature ramp. The $\nu(O\text{-}H)_{H\text{-}bond}$ and ν(C-H) regions associated with DMMP adsorption, however, exhibit a non-linear response with respect to temperature and thus the change in absorbance over these regions was attributed to the desorption of DMMP.

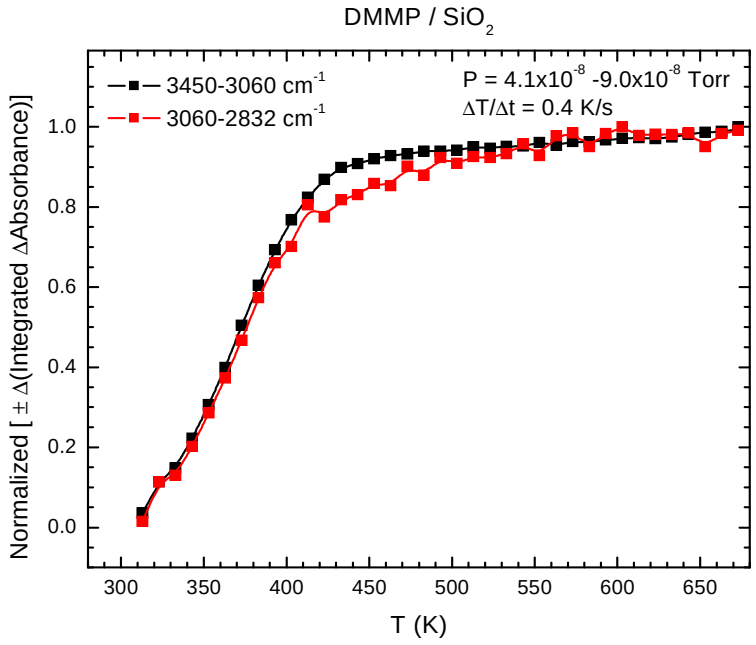

Figure 3.9: The change in integrated ΔA behavior for the $\nu(O\text{-}H)_{H\text{-}bond}$ (3450-3060 cm^{-1}) and ν(C-H) (3060-2832 cm^{-1}) DMMP adsorption regions.

To construct a TPD trace from the IR data, the change in integrated ΔA for the $\nu(O\text{-}H)_{H\text{-}bond}$ and ν(C-H) regions for each spectrum was divided by the temperature at which that spectrum was recorded and plotted with respect to the temperature, as displayed in Figure 3.10. The temperature of peak desorption was recorded to be 373 K, a difference of only 2 K compared with the conventional TPD approach using the mass spectrometer. Analysis applied to the curve exhibited an activation energy of desorption of 20 kcal/mol, the same as was determined using mass spectrometric methods. Due to the time required to collect each spectrum, the peak desorption temperature determined using infrared spectroscopy has an uncertainty of approximately ±5 K at a heating rate of 0.4 K/s, corresponding to an uncertainty in the E_a of ± 0.3 kcal/mol for this experiment. This is much less than the standard deviation in the E_a of ±3 kcal/mol that has been calculated for similar TPD experiments conducted in our laboratory. Although we have not yet investigated the precision of the instrument, we estimate the uncertainty in our measurements to be around ±3 kcal/mol.

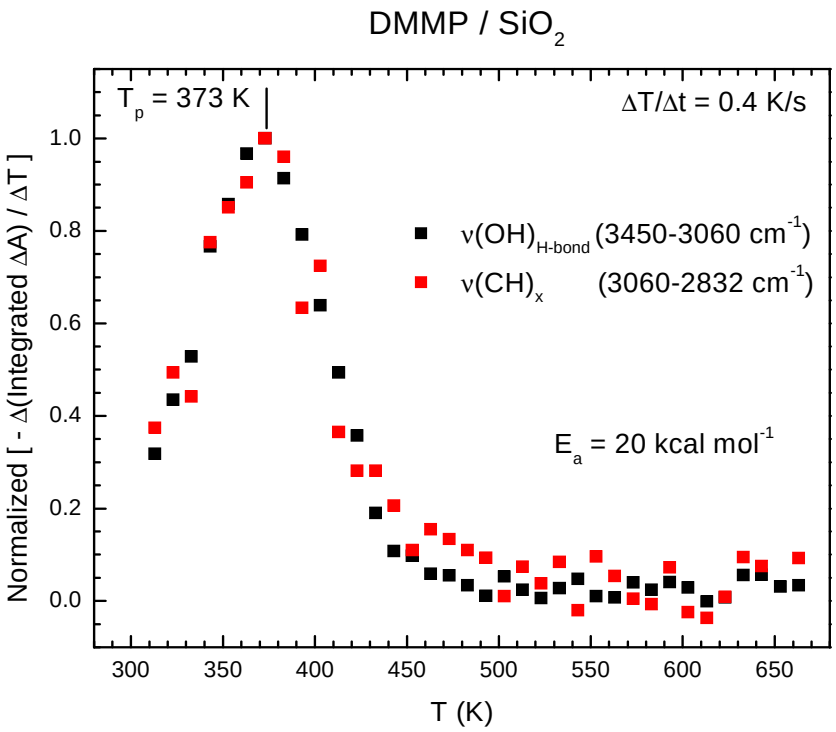

Figure 3.10: TPD trace for DMMP/SiO_2 prepared with infrared spectroscopy by following the change in absorbance at the $\nu(O\text{-}H)_{H\text{-}bond}$ and $\nu(C\text{-}H)$ regions. The change in absorbance of these modes is divided by the change in temperature to give the relative desorption rate. The desorption rate plotted with respect to the temperature produces the characteristic TPD curve and clearly depicts the temperature of peak desorption at 373 K.

Both the infrared and mass spectrometric methods give an E_a value of 20 kcal/mol. Since the desorption energy for both the mass spectrometric and infrared methods is the same, we can confirm that IR spectroscopy has been successfully applied to conduct a TPD experiment. Using IR to conduct the TPD study, we have shown that desorption of DMMP is due to breaking of hydrogen bonds between surface –OH groups and DMMP. The ν(C-H) modes decrease in absorbance due to the DMMP leaving the surface. Since the TPD profile and desorption energy

for the ν(C-H) and $\nu(O\text{-}H)_{H\text{-}bond}$ modes are the same, we can conclude that the $\nu(O\text{-}H)_{H\text{-}bond}$ modes change because of the desorption of DMMP, and thus are involved in bonding to DMMP.

Compared to Bermudez' basis set corrected ΔE_{ads} value of 20 kcal/mol,[63] the results of this study provide very strong evidence in support of the argument that DMMP binds to silica via the phosphoryl oxygen and not through the methoxy group. Bermudez posits that the elimination of the DMMP $\nu(O\text{-}CH_3)$ modes upon adsorption are due to broadening caused by coupling with the Si-O-Si lattice vibrations and not due to hydrogen bonding to the methoxy group as was concluded by Tripp et al. Although no useful information about the ν(P=O) shift was obtained from the IR spectrum due to occlusion by the SiO_2 vibrations, this study offers strong, experimental support to the conclusions of Bermudez' computational work regarding the adsorption energy and binding configuration of DMMP on silica.

3.4 Summary and Future Work

In addition to providing experimental data regarding the desorption energy of DMMP on silica, the functionality of infrared spectrometry as an analytical method for TPD experiments was demonstrated. Both IR and mass spectrometric TPD methods provided the same result for the desorption energy and provided very similar peak desorption temperatures of 375 K with the MS and 373 K with the IR. Reproduction of published E_a values (20 kcal/mol)[63] demonstrated the accuracy of the instrument. Furthermore, the TPD experiments conducted in this study proved the functionality of the new instrument. Sample temperature control, dosing, infrared spectroscopy and mass spectrometry all functioned satisfactorily during the experiment.

The instrument provides the means to perform a variety of experiments at a fraction of the time and cost of similar ultrahigh vacuum chambers. Recent efforts in our research group

have provided a method for the rapid screening of metal oxide nanoparticles with regard to their capacity to destructively sorb chemical warfare agent simulants. The instrument discussed in the present work will function as tool for intermediate level analysis of such interactions, providing high-quality results for a range of experiments at a fraction of the time and cost of the ultrahigh vacuum methods. Potentially, the small size of the chamber could allow for its installation in a fume hood where studies using actual chemical warfare agents or other toxic compounds could be safely accomplished.

It is the author's hope that experimental capacity of this instrument is not limited to the study of chemical warfare agent interactions with metal oxide nanoparticles. The simplistic but robust design of the instrument should facilitate the development and installation of new equipment, affording the possibility for expanded capabilities. Potentially, the instrument could be augmented to include other analytical methods, such as a quartz crystal microbalance or a multi-gas doser. A precision manipulator and a different sample mount design could enable studies of thin films or self-assembled monolayers. Although the instrument was designed specifically to study nanoparticulate samples, it is not difficult to envision the use of the instrument as a valuable tool to study a range of fundamental gas-surface interactions.

REFERENCES

1. Coleman, K., *A History of Chemical Warfare*. Palgrave Macmillan: New York, 2005.
2. Ali, J.; Dwyer, A.; Lewis, F. A.; Patrick, W. C.; Sidell, F. R., *Jane's Chemical-Biological Defense Guidebook*. Jane's Information Group: Alexandria, VA, 1999.
3. Tucker, J. B., *War of Nerves*. Pantheon Books: New York, 2006.
4. Tusarova, I.; Halamek, E.; Kobliha, Z., Study on reactivation of enzyme-inhibitor complexes by oximes using acetylcholine esterase inhibited by organophosphate chemical warfare agents. *Enzyme and Microbial Technology* **1999,** 25, 400-403.
5. Talmage, S. S.; Watson, A. P.; Hauschild, V.; Munro, N. B.; King, J., Chemical Warfare Agent Degradation and Decontamination. *Current Organic Chemistry* **2007,** 11, 285-298.
6. Wagner, G. W.; Procell, L. R.; O'Connor, R. J.; Munavalli, S.; Carnes, C. L.; Kapoor, P. N.; Klabunde, K. J., Reactions of VX, GB, GD, and HD with Nanosize Al_2O_3. *J. Am. Chem. Soc.* **2001,** 123, 1636-1644.
7. Yang, Y.-C., Chemical Detoxification of Nerve Agent VX. *Accounts of Chemical Research* **1998,** 32, 109-115.
8. Mitchell, M. B.; Sheinker, V. N.; Tesfamichael, A. B.; Gatimu, E. N.; Nunley, M., Decomposition of Dimethyl Methylphosphonate (DMMP) on Supported Cerium and Iron Co-Impregnated Oxides at Room Temperature. *J. Phys. Chem. B* **2003,** 107, 580-586.
9. Chen, Y.-C.; Vorontsov, A. V.; Smirniotis, P. G., Enhanced photocatalytic degradation of dimethyl methylphosphonate in the presence of low-frequency ultrasound. *Photochem. Photobiol. Sci.* **2003,** 2, 694-698.
10. Yang, Y.-C.; Baker, J. A.; Ward, J. R., Decontamination of Chemical Warfare Agents. *Chem. Rev.* **1992,** 92, 1729-1743.
11. Wagner, G. W.; Yang, Y.-C., Rapid Nucleophilic/Oxidative Decontamination of Chemical Warfare Agents. *Industrial & Engineering Chemistry* **2002,** 41, 1925-1928.
12. Bartlet-Hunt, S. L.; Knappe, D. R. U.; Barlaz, M. A., A Review of Chemical Warfare Agent Simulants for Use in Environmental Applications. *Environmental Protection Agency* **2008**.
13. Volodin, A. M.; Bedilo, A. F.; Heroux, D. S.; Zaikovskii, V. I.; Mishakov, I. V.; Chesnokov, V. V.; Klabunde, K. J. In *Surface Chemistry in Biomedical and Environmental Science*, Pure and Applied Surface Chemistry and Nanomaterials for Human Life and Environmental Protection, Kiev, Ukraine, 2006, 2005; Blitz, J. P.; Gun'ko, V., Eds. Springer: Kiev, Ukraine, 2005; pp 403-412.
14. Gordon, W. O.; Tissue, B. M.; Morris, J. R., Adsorption and Decomposition of Dimethyl Methylphosphonate on Y_2O_3 Nanoparticles. *J. Phys. Chem. C* **2007,** 111, (8), 3233-3240.
15. Klabunde, K. J.; Stark, J.; Koper, O.; Mohs, C.; Park, D. G.; Decker, S. P.; Jiang, Y.; Lagadic, I.; Zhang, D., Nanocrystals as Stoichiometric Reagents with Unique Surface Chemistry. *J. Phys. Chem.* **1996,** 100, 12142-12153.
16. Jiang, Y.; Decker, S. P.; Mohs, C.; Klabunde, K. J., Catalytic Solid State Reactions on the Surface of Nanoscale Metal Oxide Particles. *J. Catal.* **1998,** 180, 24-35.
17. Panayotov, D. A.; Morris, J. R., Catalytic Degradation of a Chemical Warfare Agent Simulant: Reaction Mechanisms on TiO_2-Supported Au Nanoparticles. *J. Phys. Chem. C* **2008**.

18. Templeton, M. K.; Weinberg, W. H., Adsorption and Decomposition of Dimethyl Methylphosphonate on an Aluminum Oxide Surface. *J. Am. Chem. Soc.* **1985,** 107, 97-108.
19. Templeton, M. K.; Weinberg, W. H., Decomposition of Phosphonate Esters Adsorbed on Aluminum Oxide. *J. Am. Chem. Soc.* **1985,** 107, 774-779.
20. Ekerdt, J. G.; Klabunde, K. J.; Shapley, J. R.; White, J. M.; Yates, J. T. J., Surface Chemistry of Organophosphorus Compounds. *J. Phys. Chem.* **1988,** 92, 6182-6188.
21. Kuiper, A. E. T.; van Bokhoven, J. J. G. M.; Medema, J., The role of heterogeneity in the kinetics of a surface reaction: I. Infrared characterization of the adsorption structures of organophophonates and their decomposition. *J. Catal.* **1976,** 43, 154-167.
22. Henderson, M. A.; Jin, T.; White, J. M., A TPD/AES Study of the Interaction of Dimethyl Methylphosphonate with α-Fe_2O_3 and SiO_2. *J. Phys. Chem.* **1986,** 90, (19), 4607-4611.
23. Mitchell, M. B.; Sheinker, V. N.; Mintz, E. A., Adsorption and Decomposition of Dimethyl Methylphosphonate on Metal Oxides. *J. Phys. Chem. B* **1997,** 101, 11192-11203.
24. Lin, S.-T.; Klabunde, K. J., Thermally Activated Magnesium Oxide Surface Chemistry. Adsorption and Decomposition of Phosphorus Compounds. *Langmuir* **1985,** 1, 600-605.
25. Rusu, C. N.; Yates, J. T. J., Adsorption and Decomposition of Dimethyl Methylphosphonate on TiO_2. *J. Phys. Chem. B* **2000,** 104, 12292-12298.
26. Obee, T. N.; Satyapal, S., Photocatalytic decomposition of DMMP on titania. *Journal of Photochemistry and Photobiology A* **1998,** 118, 45-51.
27. Ollis, D. F.; Pelizzetti, E.; Serpone, N., Photocatalyzed destruction of water contaminants. *Environmental Science & Technology* **2002,** 25, (9), 1522-1529.
28. Hidaka, H.; Zhao, J.; Pelizzetti, E.; Serpone, N., Photodegradation of Surfactants, 8. Comparison of Photocatalytic Processes between Anionic Sodium Dodecylbenzenesulfonate and Cationic Benzyldodecyldimethylammonium Chloride on the TiO_2 Surface. *J. Phys. Chem.* **1992,** 96, 2226-2230.
29. Li, Y.-X.; Klabunde, K. J., Nanoscale Metal Oxide Particles as Chemical Reagents. Destructive Adsorption of a Chemical Agent Simulant, Dimethyl Methylphosphonate, on Heat-Treated Magnesium Oxide. *Langmuir* **1991,** 7, 1388-1393.
30. Rusu, C. N.; Yates, J. T. J., Photooxidation of Dimethyl Methylphosphonate on TiO_2 Powder. *J. Phys. Chem. B* **2000,** 104, (51), 12299-12305.
31. Graven, W. M.; Weller, S. W.; Peters, D. L., Catalytic conversion of an organophosphate vapor over platinum-alumina. *Ind. Eng. Chem. Process Des. Dev.* **1966,** 5, (2), 183-189.
32. Chen, J.; Lin, J. C.; Purohit, V.; Cutlip, M. B.; Suib, S. L., Photoassisted catalytic oxidation of alcohols and halogenated hydrocarbons with amorphous manganese oxides. *Catalysis Today* **1997,** 33, 205-214.
33. Segal, S. R.; Cao, L.; Suib, S. L.; Tang, X., Thermal Decomposition of Dimethyl Methylphosphonate over Manganese Oxide Catalysts. *J. Catal.* **2001,** 198, 66-76.
34. Cao, L.; Segal, S. R.; Suib, S. L.; Tang, X.; Satyapal, S., Thermocatalytic Oxidation of Dimethyl Methylphosphonate on Supported Metal Oxides. *J. Catal.* **2000,** 194, 61-70.
35. Sheinker, V. N.; Mitchell, M. B., Quantitative Study of the Decomposition of Dimethyl Methylphosphonate (DMMP) on Metal Oxides at Room Temperature and Above. *Chem. Mater.* **2002,** 14, 1257-1268.
36. Gadgil, M. M.; Kulshrestha, S. K., $Al_{1-x}Fe_xPO_4$ Catalyst: Calcination Behavior. *J. Solid State Chem.* **1994,** 113, 15-20.
37. Decker, S. P.; Klabunde, J. S.; Khaleel, A.; Klabunde, K. J., Catalyzed Destructive Adsorption of Environmental Toxins with Nanocrystalline Metal Oxides. Fluoro-, Chloro-,

Bromocarbons, Sulfur, and Organophosphorus Compounds. *Environmental Science & Technology* **2002,** 36, (4), 762-768.
38. Wagner, G. W.; Koper, O.; Lucas, E.; Decker, S. P.; Klabunde, K. J., Reactions of VX, GD, and HD with Nanosize CaO: Autocatalytic Dehydrohalogenation of HD. *J. Phys. Chem. B* **2000,** 104, 5118-5123.
39. Wagner, G. W.; Bartram, P. W.; Koper, O.; Klabunde, K. J., Reactions of VX, GD, and HD with Nanosize MgO. *J. Phys. Chem. B* **1999,** 103, (16), 3225-3228.
40. Thompson, D., An overview of gold-catalysed oxidation processes. *Top. Catal.* **2006,** 38, (4), 231-240.
41. Boccuzzi, F.; Chiorino, A.; Manzoli, M.; Andreeva, D.; Tabakova, T., FTIR Study of the Low-Temperature Water-Gas Shift Reaction on Au/Fe_2O_3 and Au/TiO_2 Catalysts. *J. Catal.* **1999,** 188, (1), 176-185.
42. Panayotov, D. A.; Yates, J. T. J., Spectroscopic Detection of Hydrogen Atom Spillover from Au Nanoparticles Supported on TiO_2: Use of Conduction Band Electrons. *J. Phys. Chem. C* **2007,** 111, (7), 2959-2964.
43. Liu, H.; Kozlov, A. I.; Kozlova, A. P.; Shido, T.; Asakura, K.; Iwasawa, Y., Active Oxygen Species and Mechanism for Low-Temperature CO Oxidation Reaction on a TiO_2-Supported Au Catalyst Prepared from Au(PPh3)(NO3) and As-Precipitated Titanium Hydroxide. *Journal of Catalysis* **1999,** 185, (2), 252-264.
44. Min, B. K.; Friend, C. M., Heterogeneous Gold-Based Catalysis for Green Chemistry: Low Temperature CO Oxidation and Propene Oxidation. *Chem. Rev.* **2007,** 107, 2709-2724.
45. Boccuzzi, F.; Chiorino, A.; Tsubota, S.; Haruta, M., FTIR Study of Carbon Monoxide Oxidation and Scrambling at Room Temperature over Gold Supported on ZnO and TiO_2. *J. Phys. Chem.* **1996,** 100, 3625-3631.
46. Chiorino, A.; Manzoli, M.; Menegazzo, F.; Signoretto, M.; Vindigni, F.; Pinna, F.; Boccuzzi, F., New insight on the nature of catalytically active gold Sites: Quatitative CO chemisorption data and analysis of FTIR spectra of adsorbed CO and of isotopic mixtures. *J. Catal.* **2009,** 262, 169-176.
47. Chen, M.; Goodman, D. W., Catalytically Active Gold: From Nanoparticles to Ultrathin Films. *Accounts of Chemical Research* **2006,** 39, 739-746.
48. Haruta, M.; Tsubota, S.; Kobayashi, T.; Kageyama, H.; Genet, M. J.; Delmon, B., Low-Temperature Oxidation of CO over Gold Supported on TiO_2, α-Fe_2O_3, and Co_3O_4. *J. Catal.* **1993,** 144, (1), 175-192.
49. Boccuzzi, F.; Chiorino, A.; Manzoli, M.; Lu, P.; Akita, T.; Ichikawa, S.; Haruta, M., Au/TiO_2 Nanosized Samples: A Catalytic, TEM, and FTIR Study of the Effect of Calcination Temperature on the CO Oxidation. *J. Catal.* **2001,** 202, 256-267.
50. Moore, J. H.; Davis, C. C.; Coplan, M. A., *Building Scientific Apparatus*. Third ed.; Westview Press: Cambridge, Massachusetts, 2003.
51. Jansen, P.; Chandler, D. W.; Strecker, K. E., A Compact Molecular Beam Machine. *Rev. Sci. Instrum.* **2009,** 80.
52. *Building-Blocks for Vacuum Science and Technology*. MDC Vacuum Products Corporation: 1999.
53. Data Sheet - Active Pirani/cold cathode transmitter PKR 251, DN 40 CF-F. http://www.pfeiffer-vacuum.com/productPdfs/PTR26002.en.pdf (October 2011),
54. Hoffman, D. M.; Singh, B.; Thomas, J. H., *Handbook of Vacuum Science and Technology*. Academic Press: San Diego, 1998.

55. Chambers, A.; Fitch, R. K.; Halliday, B. S., *Basic Vacuum Technology*. 2 ed.; IOP Publishing: Bristol, UK, 1998.
56. O'Hanlon, J. F., *A User's Guide to Vacuum Technology*. 3 ed.; John Wiley & Sons: Hoboken, NJ, 2003.
57. Basu, P.; Ballinger, T. H.; Yates, J. T. J., Wide Temperature Range IR Spectroscopy Cell for Studies of Adsorption and Desorption on High Area Solids. *Rev. Sci. Instrum.* **1988,** 59, (8), 1321-7.
58. Hollas, J. M., *Modern Spectroscopy*. 4 ed.; John Wiley & Sons: Hoboken, NJ, 2004.
59. Aurian-Blajeni, B.; Boucher, M. M., Interaction of dimethyl methylphosphonate with metal oxides. *Langmuir* **1989,** 5, (1), 170-4.
60. Kanan, S. M.; Lu, Z.; Tripp, C. P., A Comparative Study of the Adsorption of Chloro- and Non-chloro-containing Organophosphorus Compounds on WO_3. *J. Phys. Chem. B* **2002,** 106, (37), 9576-9580.
61. Kanan, S. M.; Tripp, C. P., An Infrared Study of Adsorbed Organophosphonates on Silica: A Prefiltering Strategy for the Detection of Nerve Agents on Metal Oxide Sensors. *Langmuir* **2001,** 17, (7), 2213-2218.
62. Panayotov, D. A.; Paul, D. K.; Yates, J. T. J., Photocatalytic Oxidation of 2-Chlorethyl Ethyl Sulfide on TiO_2-SiO_2 Powders. *J. Phys. Chem. B* **2003,** 107, (38), 10571-10575.
63. Bermudez, V. M., Computational Study of the Adsorption of Trichlorophosphate, Dimethyl Methylphosphonate, and Sarin on Amorphous SiO_2. *J. Phys. Chem. C* **2007,** 111, (26), 9314-9323.
64. Kim, C. S.; Lad, R. J.; Tripp, C. P., Interaction of organophosphorous compounds with TiO_2 and WO_3 surfaces probed by vibrational spectroscopy. *Sensors and Actuators, B: Chemical* **2001,** B76, (1-3), 442-448.
65. Tripp, C. P.; Hair, M. L., Reaction of Chloromethylsilanes with Silica: A Low-Frequency Infrared Study. *Langmuir* **1991,** 7, (5), 923-927.
66. Innocenzi, P., Infrared spectroscopy of sol-gel derived silica-based films: a spectra-microstructure overview. *J. Phys. Chem. B* **2003,** 107, (20), 4711-4717.
67. Smentkowski, V. S.; Hagans, P.; Yates, J. T. J., Study of the catalytic destruction of dimethyl methylphosphonate(DMMP): oxidation over molybdenum(110). *J. Phys. Chem.* **1988,** 92, (22), 6351-6357.
68. Redhead, P. A., Thermal Desorption of Gasses. *Vacuum* **1962,** 12, 203-211.
69. Du, Z.; Sarofim, A. F.; Longwell, J. P., Activation energy distribution in temperature-programmed desorption: modeling and application to the soot oxygen system. *Energy and Fuels* **1990,** 4, (3), 293-302.
70. Masel, R. I., *Principles of Adsorption and Reaction on Solid Surfaces*. John Wiley & Sons, Inc.: Hoboken, NJ, 1996.
71. Wilmsmeyer, A.; Panayotov, D. A.; Jeffery, B.; Morris, J. R., Uptake and Desorption of CWA Simulants from Porous Silica Surfaces. **in preparation**.